

REPORT DOCUMENTATION PAGE

Form Approved
OMB No. 0704-0188

Public reporting burden for this collection of information is estimated to average 1 hour per response, including the time for reviewing instructions, searching existing data sources, gathering and maintaining the data needed, and completing and reviewing this collection of information. Send comments regarding this burden estimate or any other aspect of this collection of information, including suggestions for reducing this burden to Department of Defense, Washington Headquarters Services, Directorate for Information Operations and Reports (0704-0188), 1215 Jefferson Davis Highway, Suite 1204, Arlington, VA 22202-4302. Respondents should be aware that notwithstanding any other provision of law, no person shall be subject to any penalty for failing to comply with a collection of information if it does not display a currently valid OMB control number. PLEASE DO NOT RETURN YOUR FORM TO THE ABOVE ADDRESS.

1. REPORT DATE (DD-MM-YYYY) 20-11-2012			2. REPORT TYPE Final		3. DATES COVERED (From - To) 10/1/2009 - 9/30/2012
4. TITLE AND SUBTITLE Systematic Study of p-type Doping and Related Defects in III-Nitrides: Pathway toward a Nitride HBT					5a. CONTRACT NUMBER
					5b. GRANT NUMBER FA9550-10-1-0012
					5c. PROGRAM ELEMENT NUMBER
6. AUTHOR(S) William Alan Doolittle					5d. PROJECT NUMBER
					5e. TASK NUMBER
					5f. WORK UNIT NUMBER
7. PERFORMING ORGANIZATION NAME(S) AND ADDRESS(ES) Georgia Institute of Technology					8. PERFORMING ORGANIZATION REPORT NUMBER
9. SPONSORING / MONITORING AGENCY NAME(S) AND ADDRESS(ES) Air Force Office of Scientific Research Suite 325, Room 3112 875 Randolph Street Arlington, VA 22203-1768 Dr. James Hwang/RSE					10. SPONSOR/MONITOR'S ACRONYM(S) AFOSR
					11. SPONSOR/MONITOR'S REPORT NUMBER(S) AFRL-OSR-VA-TR-2012-1240
12. DISTRIBUTION / AVAILABILITY STATEMENT Distribution A - Approved for public release					
13. SUPPLEMENTARY NOTES					
14. ABSTRACT The group-III nitride materials system has been meticulously investigated since the late 1980s for its applications in electronic and optoelectronic devices. These materials have a direct bandgaps that are tunable from 0.7 eV (InN) to 6.2 eV (AlN) by forming alloys of the different III-nitride binaries. This bandgap range covers the entire visible spectrum, and some useful regions of ultraviolet and infrared light. In the case of light emission, this materials system boasts an enormous array of applications including indicators, lasers, solid state illumination, and water purification/sterilization among others. Group-III nitrides also have a very strong resistance to radiation damage, providing applications in space, as well.					
15. SUBJECT TERMS					
16. SECURITY CLASSIFICATION OF: a. REPORT U			17. LIMITATION OF ABSTRACT b. ABSTRACT U	18. NUMBER OF PAGES c. THIS PAGE U	19a. NAME OF RESPONSIBLE PERSON Dr. James Hwang 19b. TELEPHONE NUMBER (include area code) 703-696-7339

I. Impact and Introduction

The group-III nitride materials system has been meticulously investigated since the late 1980s for its applications in electronic and optoelectronic devices. These materials have a direct bandgaps that are tunable from 0.7 eV (InN) to 6.2 eV (AlN) by forming alloys of the different III-nitride binaries. This bandgap range covers the entire visible spectrum, and some useful regions of ultraviolet and infrared light. In the case of light emission, this materials system boasts an enormous array of applications including indicators, lasers, solid state illumination, and water purification/sterilization among others. Group-III nitrides also have a very strong resistance to radiation damage, providing applications in space, as well.

Being a direct-bandgap bandgap system, these materials can also absorb light, yielding applications in photovoltaics. Silicon solar cells have a maximum theoretical efficiency of only about 29% due to the set bandgap of the material. For these single-material, single-junction cells, some solar energy is lost by being too low in energy, passing through the device. Furthermore, some solar energy is lost by being too high in energy, losing excess energy above the bandgap of the material in the form of heat. If multiple photovoltaic devices with multiple bandgaps can be stacked and linked to each other via tunnel junctions, the maximum theoretical efficiency approaches unity. The III-nitride materials system exhibits a great advantage in the multi-junction solar cell market. Even the highest recorded efficiency GaAs-based multi-junction photovoltaics currently do not have means of absorbing the highest energy light from the solar spectrum. Aluminum containing nitrides can reach a bandgap of 6.2 eV, well within the ultraviolet region and capable of absorbing the lion's share of the sun's energy.

However, the nitride materials system is not without its challenges. Since the first reported case of p-type conductivity in GaN in 1989, there has been very little improvement in hole concentration. For 20 years after this first discovery of p-type conductivity, hole concentrations were limited to the 10^{18} cm^{-3} range. This limit has caused a wide set of difficulties in nitride-based devices. In the case of electronics, several device designs have been unfeasible due to this low hole concentration, such as heterojunction bipolar transistors. In the case of optoelectronics, light emission can be directly linked to the hole concentration of the p-type layer and corresponding hole injection efficiencies. The phenomenon known as "current droop" or "efficiency droop", where a light emitting diode decreases in efficiency for higher current densities, has even been attributed by some authors to the relatively low hole concentration in the p-type layer.

The problem lies in forcing the Mg to occupy the correct Ga-substitutional site, while still maintaining a high crystalline quality. In this study, the growth of p-GaN with hole concentrations in excess of 10^{19} cm^{-3} were characterized. It was found that for the growth techniques used by the PI, an enormous amount of Mg was occupying the correct Ga-substitutional site. This increase of electrically active Mg concentration facilitated the creation of an acceptor band instead of discrete acceptor states. Temperature-dependent electrical analysis confirmed the existence of this acceptor band by negligible carrier freeze-out at low temperatures.

Another challenge lies in the growth of InGaN alloys, which are necessary to cover the entire visible spectrum in emission and absorption. These layers exhibit a phenomenon known as phase separation. Phase separation is a process such that a heterogeneously mixed material splits into clusters of two or more phases. In the case of InGaN alloys, some of the indium may migrate into clusters of InN, depriving the rest of the film of some indium and creating a jagged bandgap structure. These clusters of high-indium content material provide charge localization centers, which are found to be very beneficial in small quantities for light emitting devices. For solar cells, these charge localization centers provide a means for charge carriers to recombine, disabling charge separation and subsequent collection.

Phase separation can occur through several different forms. In this report, we detail how each form of phase separation can be suppressed to create single-phase, high-quality InGaN layers. These layers, as described both above and herein, have an enormous immediate impact on photovoltaic and light-emitting devices.

Finally, when growing group-III nitride heterojunctions together, every grower must consider the extreme lattice mismatch between the nitride binaries. These differences in lattice spacing create a considerable amount of strain in the crystal, which forms dislocations when relaxed. In the case of only 30% indium composition InGaN grown directly on GaN, less than one monolayer of InGaN can be grown before the crystal strain relaxes, producing an enormous amount of dislocations. In the case of any device, these dislocations act as a detriment to device performance, and thus a method of mitigating or preventing dislocation propagation becomes necessary.

Herein, we discuss a transmission electron microscopy study of InGaN films towards a study of dislocation formation. It is found that very few dislocations propagate through the InGaN film, while the majority of these dislocations terminate at the GaN/InGaN interface. Although further studies are warranted and ongoing to elucidate this phenomenon, this structural analysis yields a promising result for future commercialization of high indium content InGaN-based devices.

II. Growth and Characterization of Single-Phase InGaN

Introduction

Since the realization of the blue light-emitting diode (LED),^{1,2} the nitride materials system has been meticulously investigated for its applications in optoelectronic devices. Specifically, the tunable direct bandgap of InGaN between 0.7 eV (InN) and 3.4 eV (GaN) makes this alloy particularly intriguing for both light-emitting^{3,4} and photovoltaic materials.⁵⁻⁷ High breakdown fields⁸ common among all group-III nitrides have been exploited for currently commercialized high-power electronics.⁹ These strengths could be further utilized in space applications due to the substantial radiation hardness¹⁰ of InGaN. The nitride materials system has an enormous set of potential applications, but several issues with the growth of InGaN currently hinder this extraordinary material. The current challenges with InGaN growth and potential solutions to mitigate these challenges via Metal-Modulated Epitaxy (MME) are discussed herein.

Currently, there exists no single native substrate for InGaN growth. Inherently, InN has a different lattice spacing than GaN, and thus no substrate can be completely lattice matched to all alloys of InGaN. InGaN LED structures are typically grown by metal-organic chemical vapor deposition (MOCVD) on sapphire or SiC substrates which have substantial lattice mismatches to all nitride alloys.¹¹ The dislocations created by this mismatch are partially mitigated by preparing GaN templates, which annihilate many defects by growing a thick GaN buffer.¹² This technique allows for the growth of thin, low indium content InGaN quantum wells to be grown completely strained and without relaxation on the thick GaN layers.¹³ Although the use of GaN templates only reduces dislocations in GaN for standard ~ 4 μm buffer layer thicknesses to 10^8 - 10^9 cm^{-3} , GaN-based LEDs still exhibit very high efficiencies due to localization of carriers in quantum wells.^{14,15} However, higher indium content quantum wells to push light emission further into the green region of the visible spectrum will result in strain relaxation, producing more non-radiative recombination centers. This use of GaN templates provides a solution for violet and blue LEDs, but both lower wavelength emission and more complex structures such as solar cells, HBTs, and laser diodes demand¹⁶ a new approach to substrate InGaN.

Although there are commonly used methods to circumvent lattice matching issues to utilize InGaN in violet/blue LEDs, there still exist some core material properties that make high-quality, high indium content InGaN difficult to grow. InGaN alloys tend to have some form of phase separation through three main processes: thermal decomposition, spinodal decomposition, and indium surface segregation.

Thermal decomposition must be considered for the growth of all group-III nitride materials, but is particularly troublesome for InGaN.¹⁷ The bonds between indium and nitrogen are weaker¹⁸ than that of gallium and nitrogen, so less thermal energy is required for the bonds to break. This property is particularly inconvenient in MOCVD growth, where elevated temperatures required to crack ammonia to provide nitrogen prohibit growth of high-indium content InGaN.^{19,20} Higher substrate temperatures during InGaN growth have been shown to dissociate indium from the InGaN alloy, leaving excess indium metal on the surface.²¹ A

reduction in growth temperature by any growth method reduces material quality,¹⁹ as less energy is supplied to reactant atoms to find an optimal location in the crystalline lattice. Thermal decomposition thus encourages the search for a growth method to be able to grow high-quality nitride materials at low temperature.²²

InGaN alloys have a region between InN and GaN such that, at certain temperatures and indium compositions, there is no energy barrier for phase separation. This complex phenomenon known as spinodal decomposition is described more in depth elsewhere,¹⁵ and can cause both minor indium compositional fluctuations as well as two completely separated, more energetically favorable phases. Spinodal decomposition may seem undesirable considering the effort to grow homogeneous InGaN alloys, however recent reports^{14,15,23} have shown that small amounts of phase separation in InGaN LEDs in fact drastically enhance light emission. The benefits arise in providing dense localized radiative recombination centers in higher concentrations than dislocations, which act as non-radiative recombination centers. The benefits of spinodal decomposition regrettably end there, as more complex structures such as solar cells^{5,7,10} and laser diodes¹⁶ demand both smooth band structures and very low dislocation densities. It should be noted that spinodal decomposition is considered a kinetically limited effect,¹⁵ occurring primarily on the surface as bulk diffusion in nitrides is very low. Increased growth rates are looked to as a potential solution, and have been met with some success.^{7,24,25}

Finally, there is the issue of indium surface segregation, which is perhaps the most disruptive of natural limitations of the nitride materials system. Indium surface segregation can be described as the tendency for indium atoms to preferentially migrate vertically^{17,26} along the growth front and laterally^{27,28} across the film during the growth of InGaN,²⁷ InGaAlN,²⁶ and InGaAs²⁹ alloys.

Vertical indium surface segregation has been explained by a competition between indium and gallium on the film surface, where it is more energetically favorable for gallium atoms to occupy surface sites.³⁰ The vertical surface segregation of indium has been shown to result in a decrease in indium incorporation³¹ and blurring of InGaN/GaN interfaces in quantum well growth.^{32,33} Vertical inhomogeneities in quantum wells negatively impact light emission due to wider well width,²⁶ which causes poor electron-hole wave function overlap.

Lateral segregation of indium has been explained by the higher stability of In-In bonds than In-Ga bonds,²⁸ encouraging indium to laterally aggregate³⁴ into islands if given enough time and mobility on the surface. This migration of indium adatoms into clusters on the growing surface has been shown to produce indium-rich nanostructures within the film.²⁷ Conversely to the case of vertical indium surface segregation, lateral surface segregation has been shown to drastically increase light emission from indium-bearing materials.³⁵ The quantum-dot-like nanostructures created from this form of indium surface segregation have been shown to enhance spatial carrier localization, producing radiative recombination centers.¹⁴ Indeed, this prominent form of phase separation in InGaN alloys has been hailed as the very reason group-III nitrides have greater LED efficiencies and lower sensitivities to threading dislocations than the phosphide and arsenide materials systems.¹⁶ Although beneficial for LEDs, lateral surface

segregation of indium is detrimental for nitride solar cells and laser diodes, where recombination of carriers must be minimized. A need then emerges for an ability to not only observe, but control indium surface segregation to utilize the outstanding qualities of the nitride materials system for both light-emitting and photovoltaic applications.

Indium-rich conditions have been used in the growth of AlGaN,³⁶ GaN,³⁷ and InN,³⁸ where indium adlayers have proven to be useful as a surfactant without affecting material compositions. However, for the case of InGaN, excess indium accumulation has a drastic effect on indium incorporation.^{27,30,34} At the temperatures generally used for InGaN growth, metallic indium has been shown to be difficult to remove from the growth surface *in situ*²⁶ without risking heat-induced phase separation³⁹ of the InGaN alloy. Suppression of indium surface segregation has historically been achieved by the use of nitrogen-rich growth conditions,^{17,19,37} which prohibit a metal adlayer from accumulating on the growing surface. Unfortunately, nitrogen-rich growth conditions result in a reduction in material quality⁴⁰ and surface smoothness.³²

Stoichiometric growth conditions would maximize crystal quality and surface smoothness in cases where metal adlayers cannot be accumulated. Such conditions are prohibitively difficult to achieve uniformly across large wafers at temperatures used for InGaN growth where an intermediate regime does not exist.⁴⁰ Considering GaN molecular-beam epitaxy (MBE) growth phase diagrams such as those presented by Adelmann et al.⁴¹ and Heying et al.,⁴⁰ a 5% temperature variation across the wafer has a approximately ten-fold variation in effective flux due to desorption at traditionally used growth temperatures. Thus, considering the above list of limitations associated with the growth of high-quality, single-phase InGaN, a new approach to InGaN growth and *in situ* control is needed.

The requirement of cold, fast growth with an emphasis on monitoring adlayer accumulation suggests Metal-Modulated Epitaxy as a potential growth candidate. Metal-Modulated Epitaxy (MME) is a growth technique applied to group-III nitrides in which metal fluxes are periodically shuttered while nitrogen remains constant.^{25,42-49} This technique uses metal-rich fluxes that would rapidly accumulate droplets in traditional MBE growth, taking advantage of the enhanced adlayer mobility^{37,50} provided by excess metal. The periodic shuttering of the effusion cells allows the excess metal to be consumed, providing smooth, dry surfaces required for traditional devices that demand abrupt interfaces.

Other shuttering techniques have been used in the growth of III-nitrides with the goal of obtaining droplet-regime crystal quality and subsequently removing excess metal *in situ* between layers. A modulated growth method reported by Poblenz et. al.^{51,52} involves the use of metal-rich conditions in the growth of GaN, accumulating a gallium adlayer on the growth surface and producing metal-rich growth. Both the nitrogen and gallium shutters are periodically closed and adsorbed droplets are subsequently removed from the surface by desorption at higher temperatures. Anion Modulation Epitaxy is a recently developed technique described by Goff et. al.,⁵³ and entails the shuttering of the nitrogen source, while gallium remains constant in GaN growth. This allows for the buildup of the gallium bilayer when the nitrogen source is closed while consuming the metal upon closing of the nitrogen source, producing droplet-regime crystal

growth. This strategy of growth avoids substrate temperature fluctuations resulting from changing radiation from the effusion cells, since the metal shutters are allowed to stay open. Finally, Droplet Elimination by Radical Beam Irradiation (DERI) developed by Yamaguchi et. al.^{38,54} has been demonstrated for InN growth, in which metal-rich growth is conducted. Near the end of the growth, the indium cell shutter is closed, allowing nitrogen irradiation to consume residual indium into the film producing droplet-free InN.

Metal-Modulated Epitaxy is a versatile growth technique that capitalizes on the similar growth techniques shared by all group-III nitrides. MME has been shown to provide increased crystal quality and grain sizes in AlN^{42,43} and GaN,⁴⁴⁻⁴⁹ single-phase InGaN layers throughout the miscibility gap,²⁵ and fast growth rates up to 1.3 $\mu\text{m/h}$ in GaN. This technique has wide substrate temperature ranges available for growth, where InGaN has been grown as low as approximately 400 °C²⁵ and AlN has been grown as hot as 800 °C.⁴² This large window of substrate temperatures allows MME to grow cold enough to avoid the intermediate regime, known to cause pitting in the growth surface.⁵⁵ Furthermore, adlayer desorption in the intermediate regime results in an exponential metal adsorbate dependence⁵⁶ on substrate temperature. Colder, non-intermediate regime growth thus inhibits substrate temperature related fluctuations in growth conditions.

In the case of binary nitride compounds, the use of extremely high metal fluxes rapidly accumulates excess metal droplets on the growth surface, usually on the order of 2-3 seconds after opening the cell shutter. These high fluxes quickly generate growth conditions that are then independent of further metal flux, as excess metal is then simply stored in droplets. This method thus allows for stable growth conditions regardless of moderate variations in cell temperatures. In cases where the adlayer quantity needs to be tailored to a specific amount, such as in the case of proper doping chemistries^{57,58} or prevention of surface segregation,²⁵ MME provides a new method of control in the form of shutter sequencing. Specifically, metal shutters can be closed at certain times during adlayer accumulation in order to limit the excess metal dose on the growth surface. In concert with reflection high-energy electron diffraction (RHEED) intensity analysis, this shutter modulation technique allows for observation and control of fractions of adsorbed metal monolayers and even a novel method of *in situ* growth rate determination.⁴⁹

MME has also been applied to the growth of Mg-doped GaN. In p-type GaN, a less Ga-rich gallium flux is used in order to suppress compensating N-vacancies, but these fluxes are still metal-rich enough to accumulate droplets over time. The use of cell shuttering periodically switches the growth between N-rich and Ga-rich conditions, maintaining the optimal substitutional site for Mg while still obtaining Ga-rich crystal quality.⁴⁵ This technique has been shown to significantly enhance Mg doping, resulting in hole concentrations in the 10^{19} cm^{-3} range for GaN,⁴⁷⁻⁴⁹ greatly exceeding previously perceived limits.⁵⁹ SIMS analyses of these films exhibit a drastic increase in Mg activation efficiency,⁴⁷ exceeding 50% in recent results to be included in a forthcoming publication. Temperature-dependent Hall data for p-GaN films grown by MME exhibit minimal carrier freeze-out,⁴⁸ indicating the onset of the Mott-Insulator transition.

In this study, MME is applied to the growth of InGaN in order to further understand the surface kinetics and atomic behavior of metal rich growth in InGaN. Specifically, the onset of indium surface segregation is studied to elucidate its causes and discover a way to prevent it. A quantified model correlating excess adlayer dose to surface segregation is developed. MME is then employed to grow InGaN films with varying compositions to determine the feasibility of this technique for high-quality, high indium content InGaN.

Experimental

All layers were grown in a Riber 32 MBE system using standard effusion cells for indium and aluminum, and a Veeco SUMO cell was used to supply gallium. A Veeco Unibulb plasma source was employed for nitrogen, and had a flow rate of 1.3 sccm at 350W. Growth rates were approximately 800 nm/h for all InGaN growth reported herein. To provide a uniform starting point for all studies, Lumilog MOCVD-grown GaN templates were used as substrates and were back-side sputtered with 1 μ m of Ta to provide uniform heating.⁴⁸ Substrates were cleaned in H₂SO₄:H₂O₂ (4:1) before being loaded into the introductory chamber and outgassed at 160 °C for 30 minutes.⁴⁹ All InGaN alloys were grown between 400 °C and 450 °C with metal-rich fluxes.²⁵ Metal fluxes used were normalized based on atomic number to account for ion gauge sensitivity differences between indium and gallium and were between 0.24 and 0.3×10^{-7} Torr normalized BEP.

InGaN was grown via MME using a shutter modulation scheme similar to that described previously,²⁵ which is illustrated in Figure 1. Both indium and gallium are opened and closed simultaneously, while nitrogen remains constant. This shutter scheme was used to study the RHEED response of In/Ga adlayers, and to achieve metal-rich growth of InGaN while preventing droplet buildup.

Samples were grown with differing metal shutter open times and indium to gallium ratios to characterize adatom kinetics of the growing InGaN surface. A series of samples with varied indium compositions throughout the miscibility gap of InN-GaN were grown using conditions found during the experiment.

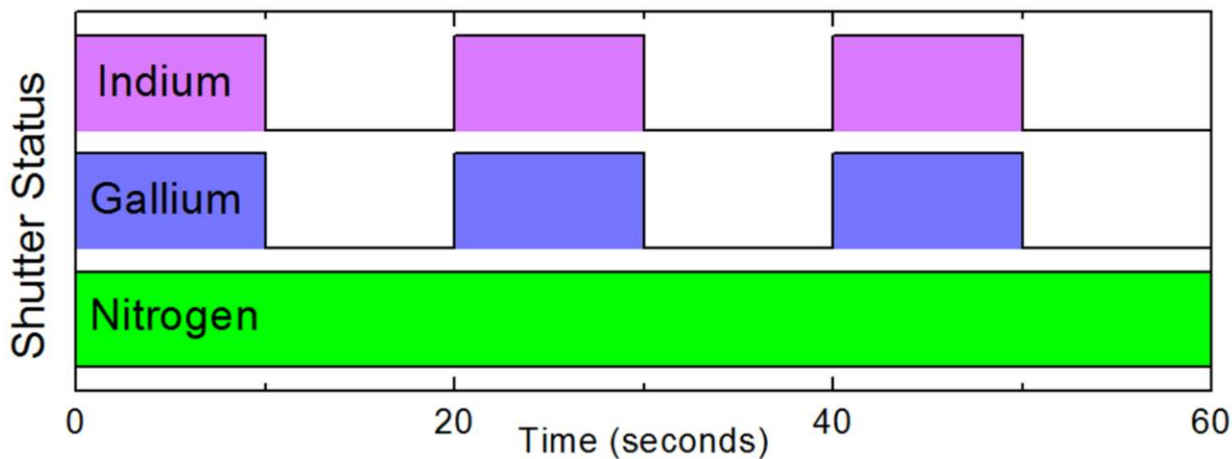


Figure 1: Simplified illustration of the modulation scheme used for the MME growth of InGaN.

Results and Discussion

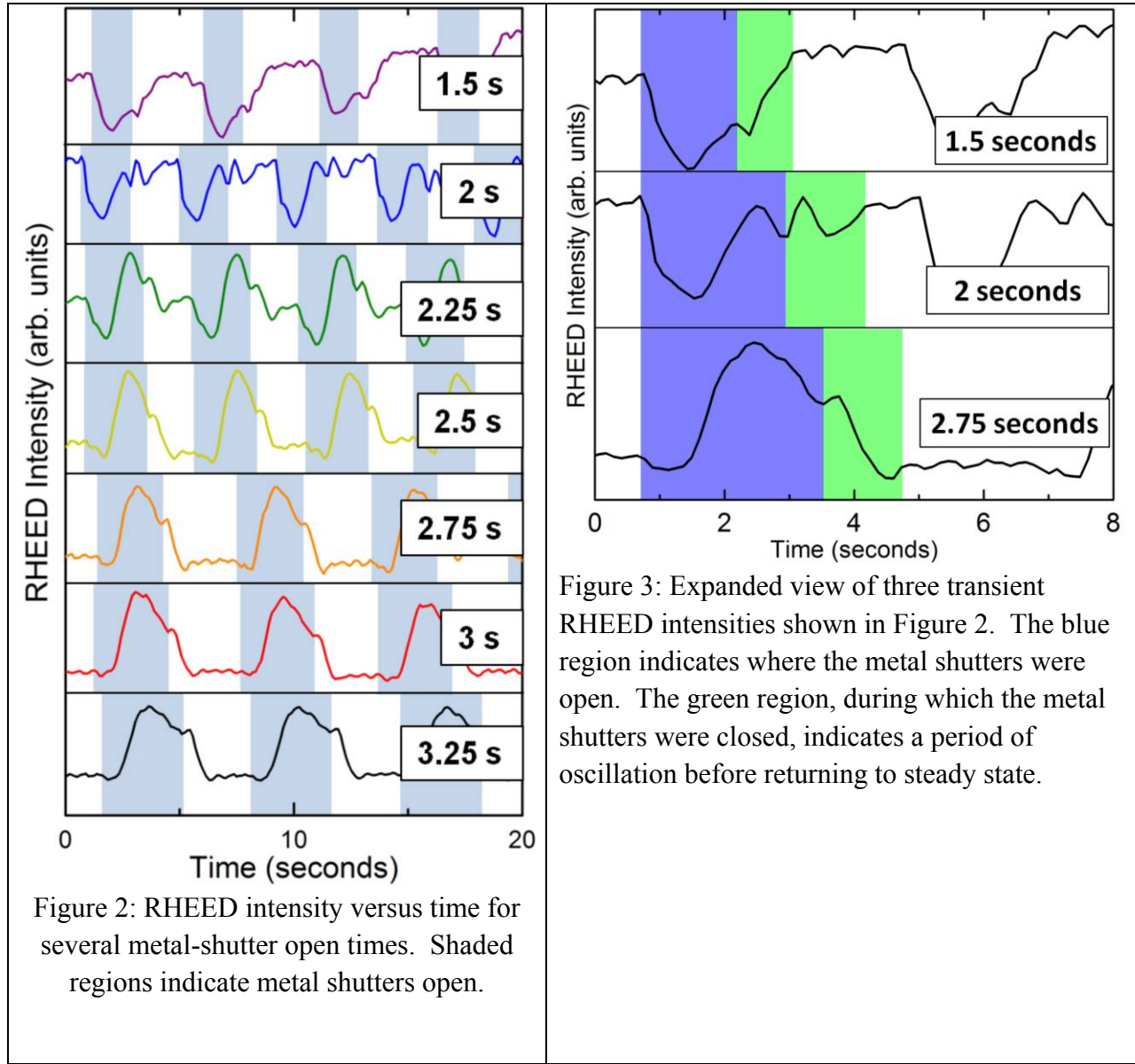
Qualification of Shuttered, Metal-rich InGaN Growth Kinetics

Previous results have shown the success of using metal-modulated epitaxy to suppress indium surface segregation in InGaN while still growing metal rich.²⁵ Although features of transient RHEED intensities during the growth of InGaN were related to indium surface segregation, association of each feature of the InGaN RHEED transient to a surface mechanism and the *in situ* quantification of indium surface segregation has until now not been reported. In Figure 2, representative RHEED transients observed during the growth of 20% InGaN for several metal shutter open times from 1.5 seconds to 3.25 seconds are shown with shaded regions indicating metal shutters open. These transient RHEED intensities were determined from one growth for consistency, with GaN interlayers grown between each InGaN layer to consume residual indium from the intentional surface segregated conditions and to provide a smooth template to facilitate comparable initial growth conditions. It is worth noting that the shutter open times shown in Figure 2 are smaller than those previously reported for similar RHEED transients, which are due to an increase in total metal flux in this present experiment. Furthermore, an enhancement of the signal-to-noise ratio in RHEED intensity collection has allowed for more detail, and thus more accurate data analysis.

Several features across all shutter open times are immediately apparent. First, a decrease of intensity on shutter open occurs, and is immediately followed by an increase in intensity. A flat, steady state intensity is also reached within a few seconds of metal shutter close which is visible across all shutter open times. Shutter-open-time-dependent features include a decreasing level of the steady-state intensity relative to a peak intensity observed during the shutter open period and an increasing width of a peak during the shutter open cycle for higher shutter open times. All of these features will be discussed in detail below. An expanded view of the 1.5 seconds, 2 seconds, and 2.75 seconds shutter open time RHEED transients are shown in Figure 3 in order to identify and explain specific features.

Shown in Figure 3 are expanded views of 3 transient RHEED signatures shown previously in Figure 2. Specific features to be discussed are colored in blue and green, where the blue region indicates metal shutter open time. The region shaded in green is a signature observed after the metal shutters are closed. Following the green region is a section of relatively flat intensity described herein as a steady state period. It is clearly seen from both Figure 2 and Figure 3 that for a given metal shutter open time in a modulation scheme, the transient RHEED intensity always begins and returns to the same intensity, regardless of truncation. If these RHEED oscillations were the result of constructive/destructive interference from the growing InGaN film,⁶⁰⁻⁶⁴ terminating the growth by closing the cell shutters at different portions of the growth cycle would result in the next open shutter cycle picking up where the previous oscillation left off. This correlation of the signature to the solid state growth of the InGaN film is not observed, and instead the intensity returns to a steady-state level after closing the metal shutters. It can then be stipulated that the transient cannot be associated with a traditional RHEED oscillation of the growing nitride film, and therefore must be dominated by the

accumulation and subsequent consumption of the metal adlayer. An oscillatory relationship between adlayer accumulation and elimination has been observed previously in the literature,^{56,65,66} and is further supported by the analysis of the signature as described below.



The reader's attention is directed to the 2 seconds metal shutter open time section of Figure 2. The white region on the left side of the figure is a flat RHEED intensity reached after a previous cycle and before metal shutters are opened that will be referred to as a steady state. Upon opening the metal shutters, an oscillatory function marked by the blue region occurs. This behavior is attributed to a RHEED oscillation associated solely on the adsorption of one metal monolayer (ML), where the minimum intensity is destructive interference caused by an incomplete layer, and the following maximum intensity is constructive interference caused by a complete layer. The remaining decrease in intensity is a continuation of this sinusoidal

oscillation as the second monolayer of metal is adsorbed, but is truncated by the closing of the metal shutters, halting the supply of metal to the surface. After the metal shutters are closed, another sinusoid that resembles the time-opposite of the blue region occurs, and is marked by the green region. This signature is attributed to the consumption of the adsorbed metal layer into the film. After the green region occurs, where adsorbed metal is consumed into the film, a steady state is again reached. An illustration of this process is shown in the non-segregated column of Figure 4, and a characteristic RHEED pattern of a sample grown under these conditions is shown in Figure 5 (a), which confirms a flat, dry surface as indicated by the bright streaks.

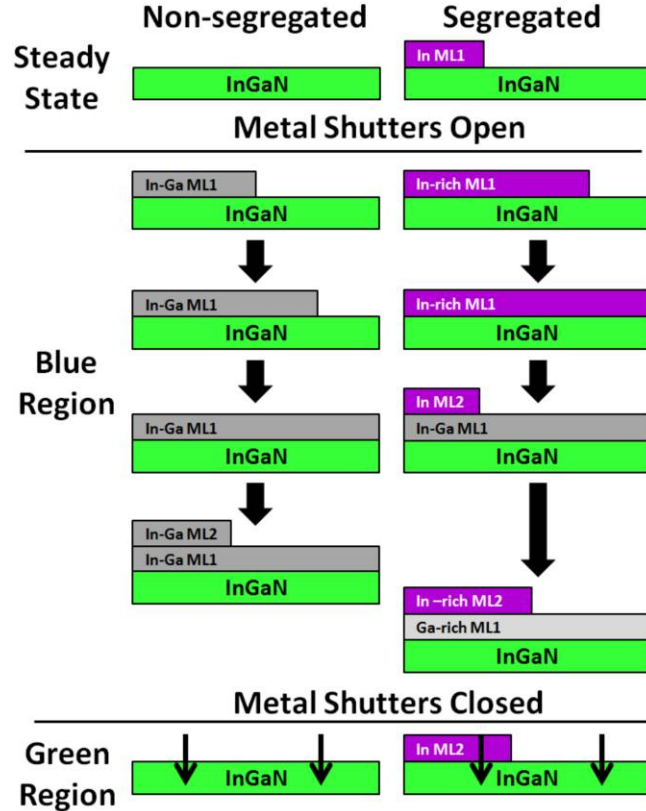


Figure 4: Illustration of the mechanism of indium surface segregation during MME of InGaN.

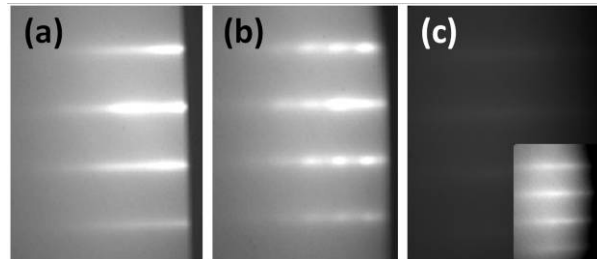


Figure 5: Characteristic RHEED patterns of InGaN grown with (a) a standard shutter open time, (b) a low shutter open time, and (c) a high shutter open time. Since the RHEED pattern of (c) is so dim that it may appear black to the reader, a brighter, contrast-enhanced version is included as an inset.

Next, the zoomed-in view of the 1.5 seconds shutter open time RHEED transient of Figure 2 is examined, and is shown at the top of Figure 3. This case is also non-surface segregated, and is similar to the 2 seconds metal shutter open time case considered above. With the use of a smaller shutter open time, a comparable RHEED oscillation is observed during the blue region after opening of the metal shutters. This oscillation similarly corresponds to the adsorption of the first monolayer of excess metal. However, the metal shutters are closed before a full oscillation takes place, which indicates truncation of excess metal accumulation before a full monolayer forms. Upon closing of the metal shutters, this excess metal is consumed into the film during the green region, and a signal that resembles the time opposite of the blue region occurs. Unfortunately, although this film exhibits no form of indium surface segregation, the lack of accumulation of a full adlayer limits the beneficial effects of the metal adlayer^{40,50} on RHEED-inferred surface smoothness. This roughness is demonstrated by both the gradual increase in RHEED intensity over time in Figure 2 and Figure 3, and the slightly spotty RHEED pattern in Figure 5(b). An illustration of this process is shown in the non-segregated column of Figure 4 excluding the bottom two steps in the blue region.

Finally, the zoomed-in view of the RHEED transient with the 2.75 second shutter open time is considered, shown in Figure 3. This case is similar to one established in a previous work to be indicative of indium surface segregated InGaN growth.²⁵ Before analyzing transient RHEED intensities of this extreme case, it is important to determine the qualitative condition of the steady state period between modulation cycles, shown by the white region on the left. In this case, so much excess metal is supplied to the adlayer in the previous modulation cycle that indium surface segregation has occurred, resulting in indium atoms riding on top of the rest of the adsorbed metal. Upon consumption of the adlayer, residual indium metal remains on the surface, as indium nitride cannot form in this system at the substrate temperatures used for these growths.²⁶ The presence of indium is supported by the diffuse RHEED pattern¹⁷ visible during the shutter closed portion of the modulation scheme, shown in Figure 5(c). With an understanding that some amount of metallic indium is present on the surface during the steady state period, an analysis of transient RHEED intensities during a growth condition with surface segregation can be performed.

Upon opening the metal shutters in the blue region of the 2.75 second shutter open time transient in Figure 3, the RHEED intensity quickly decreases to a minimum before steadily increasing again to a maximum. The time elapsed until reaching the minimum intensity is reduced in this case compared to the transients with smaller shutter open times in **Figure 2**. Furthermore, the intensity during the steady state period is also decreased. These features are consistent with the conclusion that indium is already present on the surface. The destructive interference produced by this incomplete layer results in a phase shift in the sinusoid associated with the RHEED oscillation. The behavior of the RHEED intensity after opening the metal shutters is thus attributed to an oscillatory function associated with the continued accumulation of one monolayer of excess metal. Since only indium may be present as all residual gallium

would have been consumed,¹⁷ it can be expected that this newly assembled adlayer is indium-rich, potentially forming In-rich InGaN.

The RHEED intensity then continues to increase as the first ML begins to finish. However, the analysis of the RHEED transients becomes more complex than simple constructive/destructive interference considerations when gallium begins to replace indium for surface sites. As the first ML finishes and further impinging metal cannot spread laterally, a second monolayer begins to form. In this case, incoming gallium atoms will preferentially displace indium atoms in the indium-rich first monolayer.^{17,30,31} This process provides an increase in RHEED intensity after the first monolayer forms, as gallium has been shown to scatter the RHEED beam less than indium.^{67,68} The second monolayer is also able to hold more metal than the first monolayer,^{56,65,66} which causes a decrease in frequency of the sinusoidal RHEED oscillation. These two effects produce a tall, skewed peak in the RHEED intensity just after one ML of excess metal accumulation.

The substitution of gallium for indium on surface sites will also affect the composition of the growing InGaN film, producing indium-lean material. Combined with the growth of indium-rich InGaN from a mostly indium adlayer at the beginning of the modulation scheme, this surface-segregated growth is expected to produce a multi-phase material. Evidence of composition fluctuations from similar growth conditions has been shown previously²⁵ by wide x-ray diffraction scan peaks in surface segregated samples.

After the metal shutters are closed, the RHEED signature highlighted in the green region occurs, resembling a faster, time-opposite of the blue region. Similarly to the green regions of the smaller shutter open times, this period of the transient RHEED intensity indicates consumption of adlayer material into the film. However, in this case, indium has been displaced by gallium to the second monolayer, and the adlayer as a whole is no longer homogenous. As the adlayer is consumed, the indium-lean first monolayer incorporates first,³⁷ leaving mostly indium on the surface. At the temperatures used for this growth InN cannot form in this system. This process leaves residual indium on the surface during the steady state period, which contributes to the diffuse RHEED pattern shown in Figure 5(c) and a decreased RHEED intensity shown in Figure 2 and Figure 3. An illustration of this process is shown in Figure 4 under the surface segregated column.

It is thus shown that indium surface segregation is linked to adlayer accumulation on the growth surface as opposed to metal-rich growth in general. By limiting the quantity of this adlayer, surface segregation can be inhibited and metal-rich growth of InGaN can be conducted. However, the thickness of this adlayer can be limited too much, hindering the smoothing effect of a wetting layer and resulting in a rough film as shown by the spotty RHEED pattern in Figure 5(b). It then becomes essential to identify the exact thickness of excess metal required to induce surface segregation, and adsorb as much metal as possible each modulation scheme without causing phase separation. Without further analysis, the exact transition between non-segregated conditions and segregated conditions is difficult to discern. A method of quantification of

indium surface segregation is then developed to both further understand indium surface segregation and provide a more calculable means of in situ characterization and control.

Quantification of Surface Segregation Onset Dose

Now that a mechanism describing indium surface segregation during metal-modulated epitaxy is elucidated, data can be further analyzed using methods established in previous work.⁴⁹ Specifically, the time required to consume the adlayer upon closing the metal shutters is considered. If indium surface segregation has occurred, some of the metal supplied during the metal shutter open time will not be able to incorporate into the film. This effect should result in a smaller time required to reach a steady state after the metal shutters are closed relative to a non-segregated growth condition. This experiment is performed both to determine the exact amount of metal required to induce surface segregation, herein called the surface segregation onset dose, and to strengthen the theory suggested in the qualification section above. To extract the thickness of the consumed layer, a general MBE growth equation is considered. The relationship between growth rate, incoming metal flux, adlayer accumulation, and adlayer desorption can be described with the equation

$$R_{Flux} = R_{Growth} + R_{Adlayer} + R_{Desorption}$$

where R_{Flux} is the rate of incoming flux, R_{Growth} is the rate of flux consumption by the film growth, $R_{Adlayer}$ is the rate of flux storage into excess metal adlayers, and $R_{Desorption}$ is the rate of adatom desorption from the surface. The low temperatures used for the growth of these InGaN samples allows for the assumption that desorption of the adlayer is negligible. Furthermore, when the metal shutters are closed, the incoming flux term can be eliminated which leaves

$$R_{Growth} = -R_{Adlayer}$$

This equation has been used to determine growth rate from the consumption of the known thickness of the bilayer in GaN (2.3 ML).⁴⁹ It can also be used in this case for a known growth rate to determine the thickness of an unknown adlayer on the surface of the growing InGaN film, by

$$R_{Growth} = -\left(\frac{D_{Adlayer}}{t_{accumulation}}\right) = \frac{D_{Adlayer}}{t_{consumption}}$$

where $D_{Adlayer}$ is the thickness of the incorporated adlayer, and $t_{consumption}$ is the time required to consume this adlayer. It has been calculated from calibration samples for this work that this composition of ~20% InGaN has a growth rate of approximately 800 nm/hr for a modulation scheme of 2 seconds shutter open time followed by 3 seconds shutter closed time. However, this growth rate takes into account the steady-state time reached after the consumption of excess metal, shown by the flat, unshaded regions in Figure 2 and Figure 3 where no growth occurs. Thus, this measure of growth rate is dependent on each particular modulation scheme by

including this time when no growth occurs. If the steady-state period is eliminated by only considering the time where metal is present during growth,⁴⁹ the film has been calculated to grow at approximately 900 nm/hr. This allows for a modulation-independent calculation of the thickness of the adlayer consumed into the film during the metal shutter closed period. With a known growth rate and a measurable time of adlayer consumption, the thickness of this consumed adlayer can be calculated.

The time to consume the metal adlayer, highlighted by the green region in Figure 2 and Figure 3, was monitored for 20% and 40% InGaN growth and a range of metal shutter open times. The beginning of this consumption region was marked by the closing of the metal shutters, while the end of this region was marked by the time when a flat, steady-state period was reached. The derivative of the RHEED signature was analyzed to consistently highlight the beginning of the steady-state time, where the signal would return to zero. For each metal shutter open time and targeted indium composition, several measured times to consume the excess metal were averaged and plotted in Figure 6. Error bars of 0.1 second in magnitude are included, which are associated with the 10 Hz sampling rate of the RHEED intensity detection software.

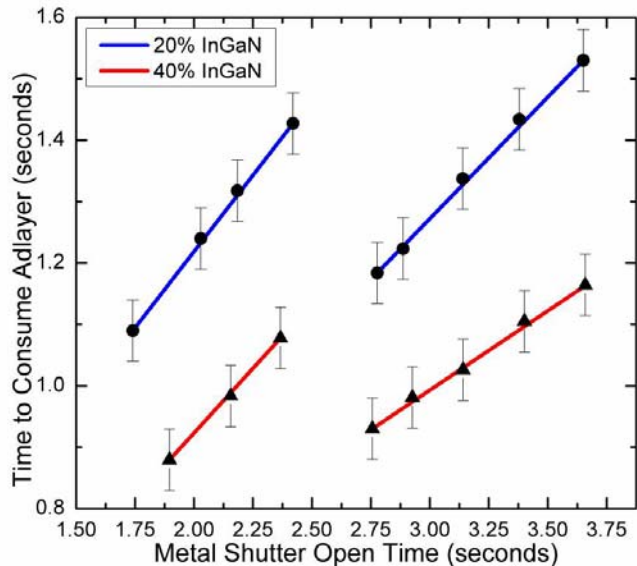


Figure 6: Time of consumption of the metal adlayer plotted versus metal-shutter open time for all conditions shown in Figure 2.

Shown in Figure 6 is the time of consumption of the metal adlayer for several metal shutter open times during the growth of 20% and 40% InGaN. For both indium compositions, the time to consume the metal adlayer increases linearly with increasing metal dose until a certain metal shutter open time. After this point, the time to consume the adlayer decreases to a lower value, then linearly increases at a different slope than before. This break in linearity is attributed to the onset of indium surface segregation, which causes indium to segregate on top of the gallium in the adlayer. In a segregated case, once the gallium-rich first monolayer of the adlayer is consumed, mostly indium remains on the surface and is prevented from incorporating

into the film due to the substrate temperature being greater than needed for InN decomposition. This would cause the steady state regions shown in Figure 2 and Figure 3 to be reached sooner since the thickness of the adlayer that can consume into the film is effectively decreased.

The decrease in time to consume the metal adlayer occurs above approximately 1.43 seconds of growth required to consume the adlayer into the film in the 20% InGaN case. By factoring in the growth rate of these films (~900 nm/hr), this growth time can be converted to a thickness of nitride film. Given the c-spacing of a 20% InGaN unit cell (0.5287 nm), the number of unit cells of InGaN grown during this time can be found. Finally, by considering that two monolayers of metal are required to produce one nitride unit cell, the number of monolayers of metal consumed during this time can be extracted.

For 20% InGaN, an adlayer thickness in excess of $\sim 1.35 \pm 0.05$ ML will result in indium surface segregation. Similarly for the 40% InGaN case, the decrease in time to consume the metal adlayer occurs above approximately 1.08 seconds of growth required to consume the adlayer into the film. Thus, an adlayer thickness in excess of 1 ± 0.05 ML will result in indium surface segregation for the growth of 40% InGaN. Above these thicknesses of excess indium and gallium adsorbed metal, herein called the surface segregation onset dose, indium atoms will segregate above gallium atoms and not incorporate during the shutter closed portion of the modulation scheme.

It is worth noting that the slopes of the trends shown in Figure 6 before and after surface segregation occurs are related by the gallium composition of the adsorbed metal. In the case of 20% InGaN, the slope of the trend after surface segregation occurs is $\sim 80\%$ of the slope of the trend before surface segregation. Similarly in the case of 40% InGaN, the slope of the trend after surface segregation is $\sim 40\%$ of the slope of the trend before surface segregation. This flux composition proportional change in the slope of the trends further strengthens the qualitative analysis stated above, such that mostly gallium incorporates while indium remains on the growth surface.

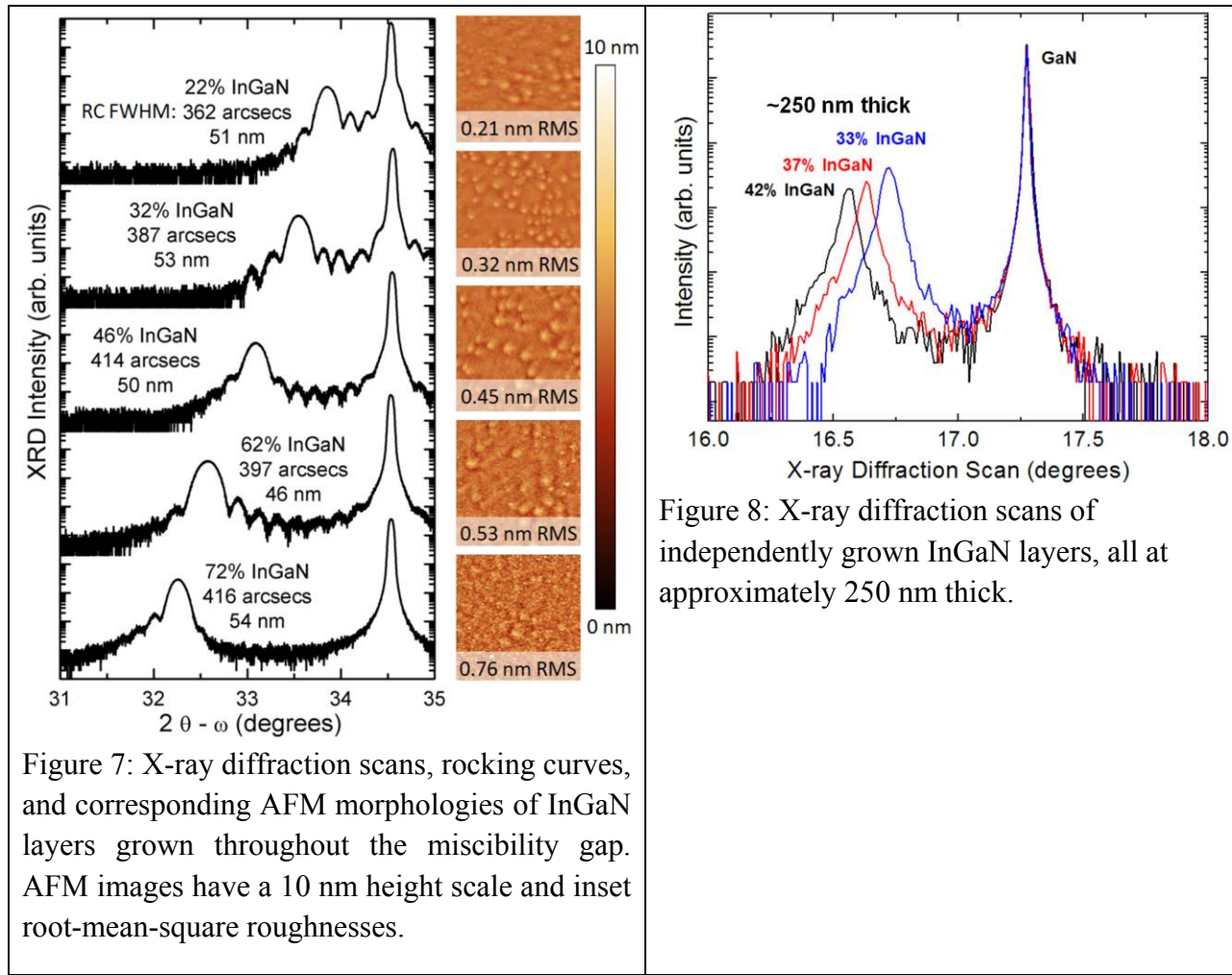
The existence of a surface segregation onset dose (1-2ML) less than the droplet accumulation thickness (2-2.5ML)^{50,56,65,66} is significant. Because an intermediate regime does not exist at these low temperatures, unshuttered MBE growth will either produce droplets or result in dry, nitrogen rich growth. Thus, some form of modulation is required for high-quality, metal-rich InGaN growth in order to accumulate a certain amount of excess metal for its beneficial effects while preventing indium surface segregation.

Application of Metal-Modulated Epitaxy to High-Indium Content InGaN

The understanding and suppression of indium surface segregation has enabled higher indium content films to be grown, well within the InN-GaN miscibility gap. Shown in Figure 7 are x-ray diffraction scans of InGaN samples with varying indium contents from 22% to 72% and associated rocking curve full widths at half maximum (FWHM) for the (0002) symmetric reflections. Atomic force microscopy images with 10 nm height scales are shown on the right with inset root-mean-square roughnesses. Film thicknesses were measured from the

Pendellösung fringes visible in the x-ray diffraction scan for all samples. Each of the samples shown in Figure 7 exhibit single phase x-ray diffraction spectra with rocking curve FWHMs comparable to the GaN templates used to substrate these films (~ 350 arcseconds).

This method was independently confirmed by Gon Namkoong at Old Dominion University for thicker InGaN layers than shown in Figure 7. Shown in Figure 8 are x-ray diffraction scans of single-phase InGaN samples, all with thicknesses of approximately 250 nm.



REFERENCES

- 1 S. Nakamura, T. Mukai and M. Senoh, Jpn. J. Appl. Phys., Part 2, **30**, L1998 (1991).
- 2 S. Nakamura, T. Mukai and M. Senoh, Appl. Phys. Lett., **64**, 1687 (1994).
- 3 T. Mukai, S. Nagahama, T. Kozaki, M. Sano, D. Morita, T. Yanamoto, M. Yamamoto, K. Akashi and S. Masui, Phys. Status Solidi A, **201**, 2712 (2004).
- 4 I. Akasaki, J. Cryst. Growth, **300**, 2 (2007).
- 5 E. Trybus, G. Namkoong, W. Henderson, S. Burnham, W. A. Doolittle, M. Cheung and A. Cartwright, J. Cryst. Growth, **288**, 218 (2006).
- 6 C. J. Neufeld, N. G. Toledo, S. C. Cruz, M. Iza, S. P. DenBaars and U. K. Mishra, Appl. Phys. Lett., **93**, 143502 (2008).
- 7 E. Trybus, O. Jani, S. Burnham, I. Ferguson, C. Honsberg, M. Steiner and W. A. Doolittle, Phys. Status Solidi C, **5**, 1843 (2008).
- 8 H. Xing, S. Keller, Y. F. Wu, L. McCarthy, I. P. Smorchkova, D. Buttary, J. J. Xu, B. P. Keller, S. P. DenBaars and U. K. Mishra, J. Phys.: Condens. Matter **13**, 7139 (2001).
- 9 U. K. Mishra, L. Shen, T. E. Kazior and Y.-F. Wu, Proc. IEEE **96**, 287 (2007).
- 10 J. Wu, W. Walukiewicz, K. M. Yu, W. Shan, J. W. Ager, E. E. Haller, H. Lu, W. J. Schaff, W. K. Metzger and S. Kurtz, J. Appl. Phys., **94**, 6477 (2003).
- 11 L. Liu and J. H. Edgar, Mater. Sci. Eng., R **37**, 61 (2002).
- 12 J. Jasinski and Z. Liliental-Weber, J. Electron. Mater., **31**, 429 (2002).
- 13 D. Holec, P. Costa, M. Kappers and C. Humphreys, J. Cryst. Growth, **303**, 314 (2007).
- 14 N. Grandjean and M. Ilegems, Proc. IEEE, **95**, 1853 (2007).
- 15 G. B. Stringfellow, J. Cryst. Growth, **312**, 735 (2010).
- 16 S. Nakamura, Semicond. Sci. Technol., **14**, R27 (1999).
- 17 C. Adelmann, R. Langer, G. Feuillet and B. Daudin, Appl. Phys. Lett., **75**, 3518 (1999).
- 18 G. Thaler, D. Koleske, S. Lee, K. Bogart and M. Crawford, Journal of Crystal Growth, **312**, (2010).
- 19 F. K. Yam and Z. Hassan, Superlattices Microstruct. , **43**, 1 (2008).
- 20 Y. Nanishi, Y. Saito, T. Yamaguchi, M. Hori, F. Matsuda, T. Araki, A. Suzuki and T. Miyajima, physica status solidi (a), **200**, 202 (2003).
- 21 I. Stanley, G. Coleiny and R. Venkat, J. Cryst. Growth, **251**, 23 (2003).
- 22 Y. Saito, N. Teraguchi, A. Suzuki, T. Araki and Y. Nanishi, Jpn. J. Appl. Phys., **40**, 91 (2001).
- 23 A. Zukauskas, K. Kazlauskas, G. Tamulaitis, P. Pobedinskas, S. Juršėnas, S. Miasojedovas, V. Y. Ivanov, M. Godlewski, C. Skierbiszewski, M. Siekacz, G. Franssen, P. Perlin, T. Suski and I. Grzegory, Phys. Status Solidi B, **243**, 1614 (2006).
- 24 Z. H. Wu, Y. Kawai, Y. Y. Fang, C. Q. Chen, H. Kondo, M. Hori, Y. Honda, M. Yamaguchi and H. Amano, Appl. Phys. Lett., **98**, 141905 (2011).
- 25 M. Moseley, J. Lowder, D. Billingsley and W. A. Doolittle, Appl. Phys. Lett., **97**, 191902 (2010).
- 26 S. Y. Karpov and Y. N. Makarov, Phys. Status Solidi A, **188**, 611 (2001).

²⁷ H. Chen, R. M. Feenstra, J. E. Northrup, T. Zywietz and J. Neugebauer, Phys. Rev. Lett., **85**, 1902 (2000).

²⁸ S. Choi, T.-H. Kim, S. Wolter, A. Brown, H. O. Everitt, M. Losurdo and G. Bruno, Phys. Rev. B, **77**, 115435 (2008).

²⁹ S. Y. Karpov and Y. N. Makarov, Thin Solid Films, **380**, 71 (2000).

³⁰ J. Neugebauer, Phys. Status Solidi C, **0**, 1651 (2003).

³¹ E. Monroy, N. Gogneau, D. Jalabert, E. Bellet-Amalric and Y. Hori, Appl. Phys. Lett., **82**, 2242 (2003).

³² O. Brandt, P. Waltereit, U. Jahn, S. Dhar and K. H. Ploog, Phys. Status Solidi A, **192**, 5 (2002).

³³ A. Dussaigne, B. Damilano, N. Grandjean and J. Massies, J. Cryst. Growth, **251**, 471 (2003).

³⁴ H. Chen, R. M. Feenstra, J. E. Northrup, T. Zywietz, J. Neugebauer and D. W. Greve, J. Vac. Sci. Technol. B, **18**, 2284 (2000).

³⁵ S. Nakamura, Science, **281**, 956 (1998).

³⁶ E. Monroy, B. Daudin, N. Gogneau, E. Bellet-Amalric, D. Jalabert and J. Brault, Phys. Status Solidi B, **234**, 726 (2002).

³⁷ J. Neugebauer, T. K. Zywietz, M. Scheffler, J. E. Northrup, H. Chen and R. M. Feenstra, Phys. Rev. Lett., **90**, 056101 (2003).

³⁸ T. Yamaguchi, D. Muto, T. Araki, N. Maeda and Y. Nanishi, Phys. Status Solidi C, **6**, S360 (2009).

³⁹ E. Hahn, A. Rosenauer, D. Gerthsen, J. Off, V. Perez-Solorzano, M. Jetter and F. Scholz, Phys. Status Solidi B, **234**, 738 (2002).

⁴⁰ B. Heying, R. Averbeck, L. F. Chen, E. Haus, H. Riechert and J. S. Speck, J. Appl. Phys., **88**, 1855 (2000).

⁴¹ C. Adelmann, J. Brault, E. Martinez-Guerrero, G. Mula, H. Mariette, L. S. Dang and B. Daudin, Phys. Status Solidi A, **188**, 575 (2001).

⁴² S. D. Burnham and W. A. Doolittle, J. Vac. Sci. Technol. B, **24**, 2100 (2006).

⁴³ S. D. Burnham, G. Namkoong, K.-K. Lee and W. A. Doolittle, J. Vac. Sci. Technol. B, **25**, 1009 (2007).

⁴⁴ S. D. Burnham, *Improved Understanding and Control of Magnesium-Doped Gallium Nitride by Plasma Assisted Molecular Beam Epitaxy*, in *Electrical and Computer Engineering*. 2007, Georgia Institute of Technology: Atlanta. p. 220.

⁴⁵ S. D. Burnham, G. Namkoong, D. C. Look, B. Clafin and W. A. Doolittle, J. Appl. Phys., **104**, 024902 (2008).

⁴⁶ S. D. Burnham, W. Henderson and W. A. Doolittle, Phys. Status Solidi C, **5**, 1855 (2008).

⁴⁷ G. Namkoong, E. Trybus, K. K. Lee, M. Moseley, W. A. Doolittle and D. C. Look, Appl. Phys. Lett., **93**, 172112 (2008).

48 E. Trybus, W. A. Doolittle, M. Moseley, W. Henderson, D. Billingsley, G. Namkoong and D. C. Look, *Phys. Status Solidi C*, **6**, S788 (2009).

49 M. Moseley, D. Billingsley, W. Henderson, E. Trybus and W. A. Doolittle, *J. Appl. Phys.*, **106**, 014905 (2009).

50 J. E. Northrup, J. Neugebauer, R. M. Feenstra and A. R. Smith, *Phys. Rev. B*, **61**, 9932 (2000).

51 C. Poblenz, P. Waltereit and J. S. Speck, *J. Vac. Sci. Technol. B*, **23**, 1379 (2005).

52 S. W. Kaun, M. H. Wong, S. Dasgupta, S. Choi, R. Chung, U. K. Mishra and J. S. Speck, *Appl. Phys. Express*, **4**, 024101 (2011).

53 L. E. Goff, C. T. Foxon, C. R. Staddon, S. V. Novikov, A. J. Kent and R. P. Campion, submitted to ICNS 2011 Proceedings, (2011).

54 T. Yamaguchi and Y. Nanishi, *Appl. Phys. Express*, **2**, 051001 (2009).

55 G. Koblmüller, J. Brown, R. Averbeck, H. Riechert, P. Pongratz and J. S. Speck, *Jpn. J. Appl. Phys., Part 2* **44**, 906 (2005).

56 J. S. Brown, G. Koblmüller, F. Wu, R. Averbeck, H. Riechert and J. S. Speck, *J. Appl. Phys.*, **99**, 074902 (2006).

57 C. Munasinghe, A. Steckl, E. E. Nyein, U. Hommerich, H. Peng, H. Everitt, V. Dierolf and J. Zavada, *Mater. Res. Soc. Symp. Proc.*, **866**, 41 (2005).

58 C. Munasinghe and A. J. Steckl, *Thin Solid Films*, **496**, 636 (2006).

59 M. McLaurin, T. E. Yates and J. S. Speck, *Appl. Phys. Lett.*, **86**, 262104 (2005).

60 C. E. C. Wood, *Surf. Sci.*, **108**, L441 (1981).

61 J. J. Harris, B. A. Joyce and P. J. Dobson, *Surf. Sci.*, **103**, L90 (1981).

62 Y. Moriyasu, H. Goto, N. Kuze and M. Matsui, *J. Cryst. Growth*, **150**, 916 (1995).

63 B. Daudin and F. Widmann, *J. Cryst. Growth*, **182**, 1 (1997).

64 W. Braun, L. Daueritz and K. H. Ploog, *Phys. Rev. Lett.*, **80**, 4935 (1998).

65 C. Adelmann, J. Brault, G. Mula and B. Daudin, *Phys. Rev. B*, **67**, 165419 (2003).

66 C. S. Gallinat, G. Koblmüller, J. S. Brown and J. S. Speck, *J. Appl. Phys.*, **102**, 064907 (2007).

67 S. Martini, A. A. Quivy, E. C. F. d. Silva and J. R. Leite, *Appl. Phys. Lett.*, **81**, 2863 (2002).

68 S. Martini, A. A. Quivy, T. E. Lamas, M. J. d. Silva, E. C. F. d. Silva and J. R. Leite, *J. Cryst. Growth*, **251**, 101 (2003).

II. Growth and Characterization of Deeply-Degenerate p-GaN

Introduction

Group III-nitride semiconductors possess a number of excellent properties which make them viable for a broad range of electronic and optoelectronic devices. These properties include a tunable, direct bandgap of $\sim 0.7 - 6.1$ eV, high drift velocity, high mobility, and strong light absorption.¹⁻³ Together these attributes make III-nitrides suited for light-emitting diodes (LEDs), high electron mobility transistors (HEMTs), and potentially solar cells and heterojunction bipolar transistors (HBTs).^{4,5} However, p-type doping of III-nitrides, a key component for many devices, remains extremely challenging. Typical hole concentrations for p-type GaN in literature are on the order of 10^{17} - 10^{18} cm⁻³, and some of the highest reported hole concentrations barely exceed 10^{18} cm⁻³ for GaN grown on c-plane sapphire.⁶ The low hole concentrations are attributed to the large activation energy of the magnesium dopant atom, often reported to be 140 – 220 meV which lead to poor ionization efficiencies of 1-5% at the highest doping concentrations.^{6,7}

The inability to achieve higher p-type doping is one possible cause of the efficiency droop seen in nitride-based LEDs,^{8,9} and directly prevents the formation of a tunnel junction critical to multi-junction solar cells. In addition, high p-type contact and base access resistance has been cited as a primary cause of performance limitations in nitride HBTs.¹⁰ These performance limitations might be alleviated by improved p-type doping. In recent years, higher hole concentrations and reduced resistivities in p-type GaN have been reported using a modified form of molecular beam epitaxy (MBE) called Metal-Modulated Epitaxy (MME).^{11,12} The details of this shuttered technique have been explored in previous publications.¹³ Growth of p-type GaN by MME has led to room temperature hole concentrations in excess of 10^{19} cm⁻³ and room temperature resistivities below 0.3 $\Omega\text{-cm}$.^{14,15} This present study demonstrates improvements in p-type conductivity and insight into the temperature-dependent properties of p-type GaN films grown by MME, and suggests impurity band conduction as the physical mechanism responsible for these improvements in the p-type electrical properties.

Experimental

All films in this paper were grown by Metal-Modulated Epitaxy in a Riber 32 MBE reactor with a base pressure of 1×10^{-10} Torr. The substrate used for all films was 1x1cm single-side polished c-plane sapphire with 2 μ m tantalum backside metal. Substrates were outgassed at 300°C for 30 minutes prior to growth. Low-temperature nitridation of the sapphire substrate was performed at 200°C for 60 minutes.¹⁶⁻¹⁹ Compared to high-temperature nitridation, low-temperature nitridation has been shown to result in higher quality, homogeneous AlN layers leading to improved GaN films.¹⁶⁻¹⁹ Reactive nitrogen species were supplied by a Veeco UNI-Bulb RF plasma source operating at 350W RF power and 1.3 sccm N₂ flow. Following low-temperature nitridation, a 100nm AlN buffer layer was grown via MME at 700°C to provide a Al-polar surface for subsequent growth.^{18,20-23} The aluminum flux during the buffer layer growth was 6×10^{-7} Torr beam equivalent pressure (BEP), and the aluminum shutter cycle was

10s open/10s closed. After growth of the AlN buffer layer, the substrate temperature was reduced to 600°C for growth of p-type GaN:Mg films. Magnesium was delivered by a Veeco corrosive series valved cracker with a bulk temperature of 280 – 300°C and a valve opening of 120 mils.²⁴ No unintentionally doped or n-doped GaN layers were grown so as to ensure all electrical measurements resulted from only the p-type GaN. Gallium was supplied by either a standard effusion cell or a Veeco SUMO® cell at a metal-rich flux of 6.5×10^{-7} to 7.5×10^{-7} Torr BEP. Gallium and magnesium were shuttered simultaneously with a cycle of 5s open/10s closed. Reflection High Energy Electron Diffraction (RHEED) was performed in-situ to aid in determining the optimal III-V flux ratio for doping as described by Namkoong et al.¹⁴ A summary of the varied growth conditions is shown in Table I. It is important to note that, due to effusion cell design and flux gauge geometric considerations, the stoichiometric flux for Ga is different between the two types of effusion cells leading to different III/V ratios for a fixed N-plasma condition. As such, the approximate III-V ratios determined from the flux resultant in Ga droplet formation are also shown in Table I to clarify the two different metal-rich conditions.

TABLE I. P-type GaN:Mg growth conditions.

	<i>Effusion Cell Type</i>	<i>Ga Flux (Torr)</i>	<i>III/V ratio</i>	<i>Mg Bulk Temp</i>	<i>Growth Time</i>
<i>Sample A</i>	standard	7.5×10^{-7}	~1.6	280°C	40 mins
<i>Sample B</i>	SUMO®	6.5×10^{-7}	~1.1	300°C	30 mins

Structural characterization was performed after growth by x-ray diffraction (XRD) using a Philips X’Pert Pro MRD equipped with a high resolution goniometer. Surface morphology was determined by a Veeco Dimension 3100 atomic force microscope (AFM) operating in tapping mode. Electrical properties of the p-type GaN films were determined using a custom temperature-dependent Hall-effect system. The Hall system consisted of a MMR Joule-Thomson thermal stage operating from 77K to 400K under a Walker Scientific two Tesla electromagnet and high-precision Keithley electronics including a model 2128A nanovoltmeter, model 7001 switch matrix with Hall measurement card, and model 6221 current source operating in DC mode. The Hall effect measurement procedure follows ASTM Standard F76.²⁵ In addition, the Hall measurement was performed inside a dark chamber to prevent any light from reaching the sample. Given the unusually high hole concentrations reported herein, previous samples were verified externally to insure no systematic error in the Hall measurements. Measurements in our lab agreed to within 5% to that measured elsewhere and these results have been previously published.¹⁵ Representative samples were also sent out to be analyzed using secondary ion mass spectrometry (SIMS) to determine Mg incorporation in MME grown p-type GaN films.

Results and Discussion

The p-GaN thickness of Sample A found by contact profilometry was approximately 300 nm after subtracting out the thickness of the insulating AlN buffer. The p-GaN thickness of Sample B was 100 nm. For heavily Mg-doped films grown by MME the full width at half maximum (FWHM) of the (0002) omega rocking curve is typically on the order of 1000 to 1500 arcseconds.¹⁵ Often attributed to the typically nitrogen-rich growth conditions, Mg doping of MBE-grown GaN films has been shown to degrade the crystal quality detected by XRD.²⁶⁻²⁸ In the case of these two MME-grown samples, a time-average nitrogen rich condition is maintained even though the instantaneous (shutter open for 1/3 duty cycle) condition is Ga-rich. As such, the relatively broad FWHM exhibited by these films, approximately 3-4 times normal for MME-grown undoped or Si-doped GaN films, are not unexpected given the time-average nitrogen rich growth conditions and unusually high doping levels in excess of $1-2 \times 10^{20} \text{ cm}^{-3}$ as determined by SIMS.¹⁵

The AFM surface morphology of a p-type GaN:Mg grown by MME with room temperature hole concentration of 1.6×10^{19} is shown in Figure 9. The film exhibits a grainy morphology with RMS roughness of 1.3 nm. This rough surface is also attributed to the large concentration of Mg dopants in the film and the time-average nitrogen rich growth conditions used for optimal p-type doping.¹⁴ For comparison, an RMS roughness on the order of 0.5-2 nm is typical for lighter-doped GaN:Mg films grown by MOCVD and traditional MBE.^{29, 30} Undoped and Si-doped MME films typically show lower than 0.5 nm RMS roughness comparable to other growth techniques but achievable at relatively lower substrate temperatures.

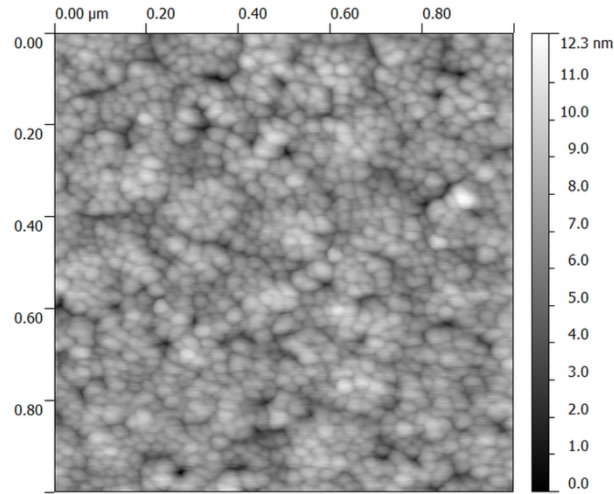


Figure 9: 1x1 μm AFM of p-type GaN:Mg film (RMS roughness = 1.27 nm).

Shown in Figure 10(a)-(d) respectively are the temperature-dependent resistivity, Hall mobility, Hall carrier concentration, and Hall coefficient for the two p-type GaN films grown by MME with slightly differing Ga and Mg flux. A full study showing the sensitivity of hole concentrations to these parameters will be presented in a later paper. These two representative samples grown under different conditions are presented to compare the electrical behavior of

traditional low 10^{18} cm^{-3} hole concentration materials to those having hole concentrations in excess of 10^{19} cm^{-3} . Differences in electrical response are observed not only in hole concentration but also in the relative levels of compensation, an important mechanism needed to understand the limitations in traditional doping.

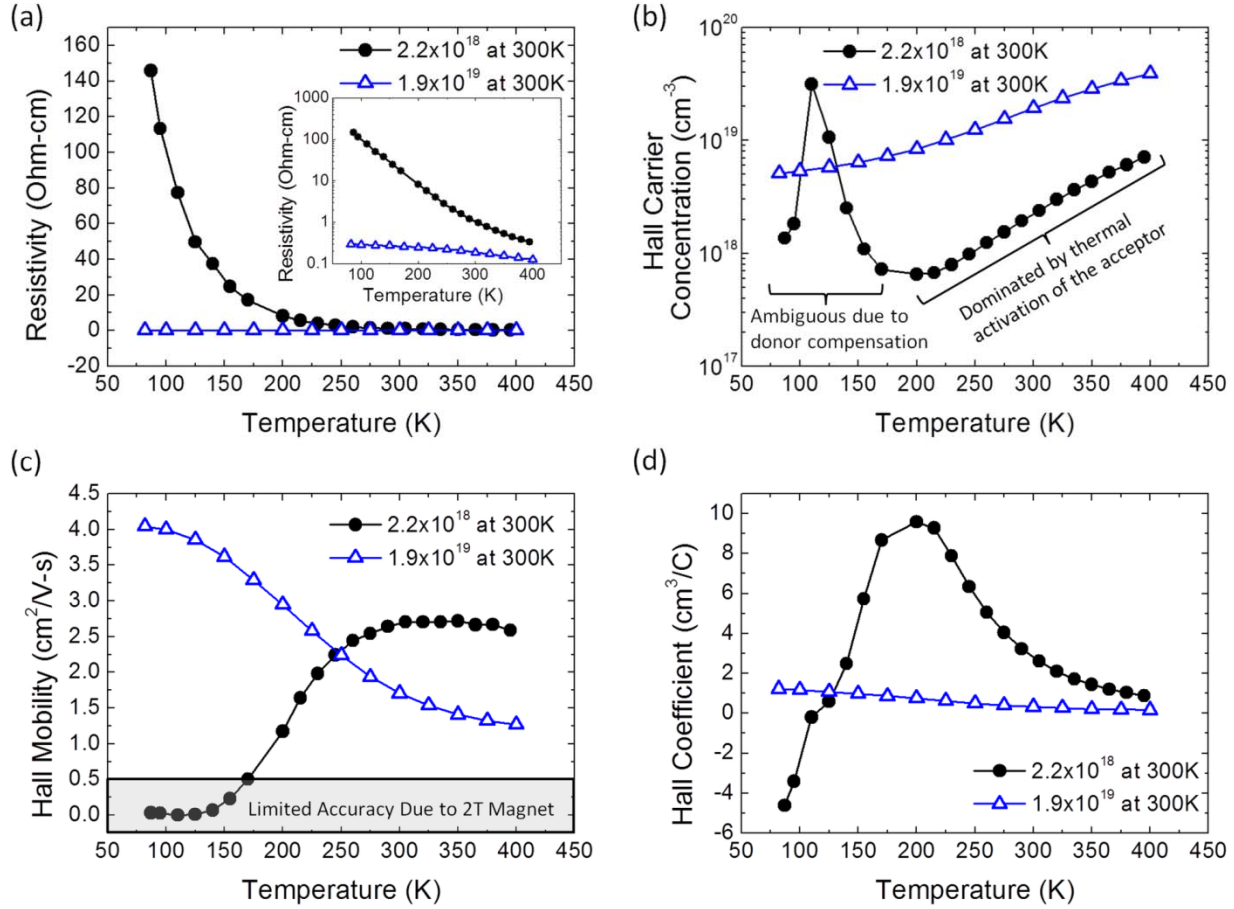


Figure 10: Temperature-dependent resistivity (a, log plot inset), Hall carrier concentration (b), Hall mobility (c), and Hall coefficient (d) for comparative p-GaN films.

It is clear from Figure 10(a)-(d) that the different growth conditions lead to dramatically different electrical properties in the two films. In Figure 10(a), Sample A exhibits classical carrier freeze-out, resulting in high resistivity. However, as the thermally activated acceptors freeze out with decreasing temperature, compensating donors begin to have more effect on the conduction. This is evident in Figure 10(b) and Figure 10(d) where, at approximately 200K, the slope of the Hall coefficient turns positive and there is a misleading rise in the calculated Hall carrier concentration. At approximately 125K the Hall coefficient approaches zero indicating complete compensation. In this temperature range there is a corresponding asymptote in the Hall carrier concentration due to the inverse relationship between Hall carrier concentration and Hall

coefficient, resulting in the misleading rise in the Hall carrier concentration. The calculated Hall carrier concentration in this temperature range should not be considered valid due to the dominance of compensation and the resultant artifacts in the Hall measurement. Below 125K the Hall coefficient is negative, indicating n-type conductivity due to the holes having frozen out below the level of compensating donors, estimated to be in the upper 10^{17} cm^{-3} range. An additional measurement consideration is that at approximately 175K the Hall mobility in Figure 10(c) drops below the detectable limit allowed by the two Tesla magnetic field (mobility μ must be greater than $1/B$, where B is the magnetic field measured in Tesla).³¹ As such, any mobility data points below 175K should be approached with caution due to this accuracy limitation set by the hardware.

In contrast, Sample B exhibits very different electrical properties versus the lighter doped sample A, and its resistivity shows very little temperature dependence at all. For reference, the resistivity of Sample B is $0.19 \Omega\text{-cm}$ at 300K and only $0.30 \Omega\text{-cm}$ at 82K. In addition, the Hall mobility of Sample B increases from $1.7 \text{ cm}^2/\text{V}\cdot\text{s}$ at 300K to $4.0 \text{ cm}^2/\text{V}\cdot\text{s}$ at 82K. Finally, the hole concentration of Sample B only drops by a factor of 3.8, from $1.9 \times 10^{19} \text{ cm}^{-3}$ at 300K to $5.1 \times 10^{18} \text{ cm}^{-3}$ at 82K. This negligible carrier freeze out at cryogenic temperatures is not characteristic of even the most heavily doped p-type GaN:Mg films grown by traditional MBE or MOCVD which typically show a temperature dependence similar that of Sample A.^{26, 30} The effective activation energy extracted from the temperature dependent hole concentration in the upper temperature regime for the highly doped Sample B was calculated to be just 70 meV, compared to the 140 – 220 meV commonly reported. It is important to note that, due to the proposed mechanism of an acceptor band discussed below, rather than a single acceptor energy level, the traditional calculation of activation energy is not accurate for very heavily doped films and is presented here merely for the purposes of qualitative comparison. In addition, the Hall scattering factor was assumed to be 1 for these measurements and does not account for any differences in the scattering factor due to conduction within an impurity band. While the scattering factor for an impurity band is unknown, generally the scattering factor for various known mechanisms results in a possible error no greater than a factor of 2.

A separate set of growths with varied room temperature hole concentrations are shown in Figure 11. In this Arrhenius plot of natural log of resistivity vs. $1000/T$, there is a clear trend in the temperature-dependent electrical properties as the hole concentration changes. The sample with $2.9 \times 10^{18} \text{ cm}^{-3}$ room temperature hole concentration has a resistivity of $155 \Omega\text{-cm}$ at 86K, while the sample with $8.0 \times 10^{18} \text{ cm}^{-3}$ hole concentration only has a resistivity of $11.6 \Omega\text{-cm}$ at 87K. This $2.75\times$ increase in room-temperature hole concentration leads to a full order of magnitude improvement in the low-temperature resistivity. The third sample with $2.8 \times 10^{19} \text{ cm}^{-3}$ hole concentration takes this improvement further still with a resistivity of just $1.5 \Omega\text{-cm}$ at 87K.

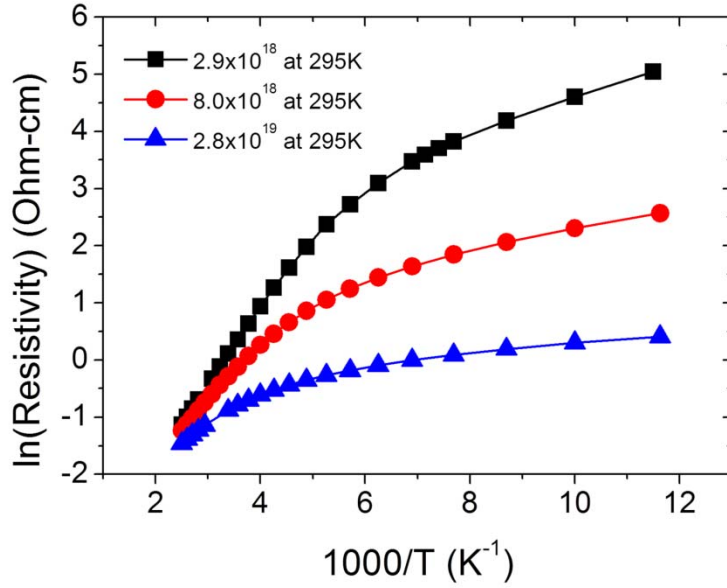


Figure 11: Trend of temperature-dependent resistivity for three samples with different room temperature hole concentrations.

In addition to the trend in low-temperature resistivity, there is also a similar trend in effective activation energy. As the hole concentration increases, the effective activation energy decreases. From the lowest to highest hole concentration (top to bottom in Figure 11), the effective activation energies, calculated from the high temperature regime of the temperature-dependent hole concentration, are 111 meV, 55 meV, and 43 meV respectively. While all of these values are lower than those typically reported in literature, the trend illustrates the important relationship between this effective activation energy and the hole concentration. This trend along with the negligible carrier freeze out shown in Figure 10 implies the formation of an acceptor band as opposed to the traditional isolated acceptor.

Representative samples were also sent for SIMS analysis. A previous publication¹⁵ reported high Mg acceptor ionization efficiencies of 10% grown by MME. Figure 12 shows a sample with Mg concentration of $1.3 \times 10^{20} \text{ cm}^{-3}$ and a room temperature hole concentration of $6.7 \times 10^{19} \text{ cm}^{-3}$ leading to a Mg acceptor ionization efficiency of approximately 52%.

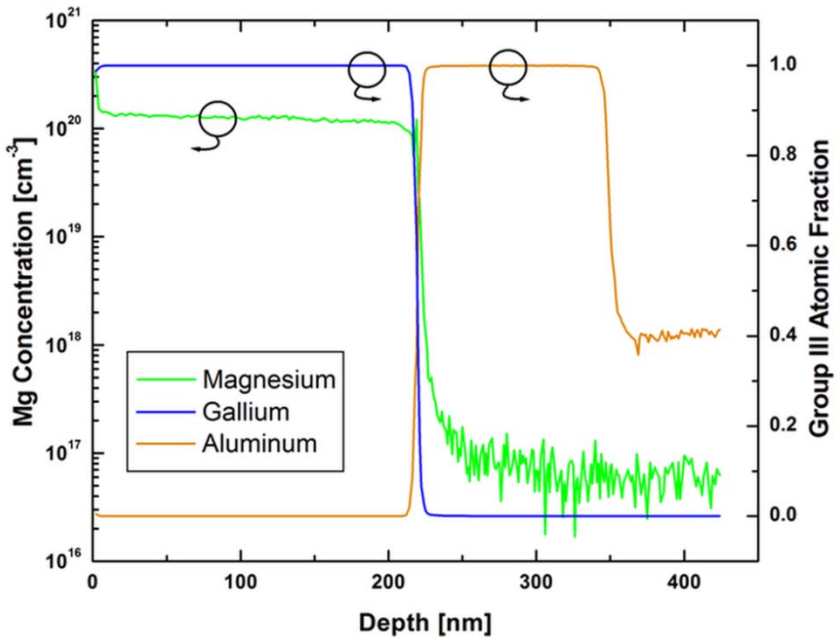


Figure 12: SIMS depth profile for MME-grown GaN:Mg film with 52% Mg activation.

Together, the temperature dependent behavior of Sample B, low activation energy, and unusually high Mg concentration in the film point to the onset of an impurity band. As the electrically active acceptor concentration increases, the isolated deep acceptor energies begin to interact and must, according to the Pauli Exclusion Principle, split into a band of states. This band formation is predicted by Mott³²⁻³⁴ to occur when the active acceptor concentration exceeds approximately $(0.2/a_H)^3$, on the order of 10^{20} cm^{-3} for GaN, where a_H is the Bohr radius for a hole. This results in the Fermi-energy becoming pinned inside the acceptor band which leads to the negligible temperature dependence of the electrical properties as evident in the highly doped case in Figure 10. As the concentration of electrically active acceptors, ionized Mg located on the proper Ga-substitutional site, increases the acceptor energy splitting pushes this acceptor band closer toward the valence band lowering the effective activation energy. It is important to note that the conduction is through free carriers in the impurity band which has minimal temperature dependence as opposed to hopping conductivity which has an $(1/T)$ temperature dependence^{33, 34} that does not fit the data. Without the formation of an impurity band and the associated reduction in effective activation energy, this large activation efficiency of 52% is not possible at room temperature for a single isolated deep acceptor traditionally found in p-type GaN. This traditional impossibility results from the Fermi-level in p-type GaN being far below the acceptor energy resulting in significant emptying of the acceptor state. The 43 to 70 meV effective activation energy is in line with that reported in a previous publication,¹⁵ but the low-temperature resistivity has been improved by over an order of magnitude due to more optimized growth conditions. Growth conditions optimized for higher hole concentration, which will be

explored in detail in a future study, result in a best hole concentration of nearly $7.9 \times 10^{19} \text{ cm}^{-3}$ but a slightly inferior resistivity of $0.26 \Omega\text{-cm}$.

REFERENCES

- ¹Y. Nanishi, Y. Saito and T. Yamaguchi, *Jpn. J. Appl. Phys.*, **42**, 2549 (2003).
- ²N. S. Mansour, K. W. Kim and M. A. Littlejohn, *J. Appl. Phys.*, **77**, 2834 (1995).
- ³J. Kolník, I. H. Oğuzman, K. F. Brennan, R. Wang, P. P. Ruden and Y. Wang, *J. Appl. Phys.*, **78**, 1033 (1995).
- ⁴S. Nakamura, *Phys. Status Solidi A*, **176**, 15 (1999).
- ⁵O. Jani, I. Ferguson, C. Honsberg and S. Kurtz, *Appl. Phys. Lett.*, **91**, 132117 (2007).
- ⁶A. Bhattacharyya, W. Li, J. Cabalu, T. D. Moustakas, D. J. Smith and R. L. Hervig, *Appl. Phys. Lett.*, **85**, 4956 (2004).
- ⁷M. Zhang, P. Bhattacharya, W. Guo and A. Banerjee, *Appl. Phys. Lett.*, **96**, 132103 (2010).
- ⁸J. Xie, X. Ni, Q. Fan, R. Shimada, Ü. Özgür and H. Morkoç, *Appl. Phys. Lett.*, **93**, 121107 (2008).
- ⁹X. Li, X. Ni, J. Lee, M. Wu, Ü. Özgür, H. Morkoç, T. Paskova, G. Mulholland and K. R. Evans, *Appl. Phys. Lett.*, **95**, 121107 (2009).
- ¹⁰T. Chung, J. Limb, J.-H. Ryou, W. Lee, P. Li, D. Yoo, X.-B. Zhang, S.-C. Shen, R. D. Dupuis, D. Keogh, P. Asbeck, B. Chukung, M. Feng, D. Zakharov and Z. Lilienthal-Weber, *J. Electron. Mater.*, **35**, 695 (2006).
- ¹¹S. D. Burnham and W. A. Doolittle, *J. Vac. Sci. Technol. B*, **24**, 2100 (2006).
- ¹²S. D. Burnham, W. Henderson and W. A. Doolittle, *Phys. Status Solidi C*, **5**, 1855 (2008).
- ¹³M. Moseley, D. Billingsley, W. Henderson, E. Trybus and W. A. Doolittle, *J. Appl. Phys.*, **106**, 014905 (2009).
- ¹⁴G. Namkoong, E. Trybus, K. K. Lee, M. Moseley, W. A. Doolittle and D. C. Look, *Appl. Phys. Lett.*, **93**, 172112 (2008).
- ¹⁵E. Trybus, W. A. Doolittle, M. Moseley, W. Henderson, D. Billingsley, G. Namkoong and D. C. Look, *Phys. Status Solidi C*, **6**, S788 (2009).
- ¹⁶G. Namkoong, W. A. Doolittle, A. S. Brown, M. Losurdo, P. Capezzuto and G. Bruno, *J. Appl. Phys.*, **91**, 2499 (2002).
- ¹⁷M. Losurdo, P. Capezzuto, G. Bruno, G. Namkoong, W. A. Doolittle and A. S. Brown, *J. Appl. Phys.*, **91**, 2508 (2002).
- ¹⁸G. Namkoong, W. A. Doolittle, A. S. Brown, M. Losurdo, M. M. Giangregorio and G. Bruno, *J. Cryst. Growth*, **252**, 159 (2003).
- ¹⁹G. Namkoong, W. A. Doolittle, S. Kang, H. Sa, A. S. Brown and S. R. Stock, *MRS Internet J. Nitride Semicond. Res.*, **5**, 1 (2000).
- ²⁰X. Q. Shen, T. Ide, S. H. Cho, M. Shimizu, S. Hara, H. Okumura, S. Sonoda and S. Shimizu, *J. Cryst. Growth*, **218**, 155 (2000).
- ²¹D. Huang, P. Visconti, K. M. Jones, M. A. Reschchikov, F. Yun, A. A. Baski, T. King and H. Morkoç, *Appl. Phys. Lett.*, **78**, 4145 (2001).

²²M. Losurdo, P. Capezzuto, G. Bruno, G. Namkoong, W. A. Doolittle and A. S. Brown, Phys. Status Solidi A, **2**, 561 (2001).

²³G. Namkoong, W. A. Doolittle, A. S. Brown, M. Losurdo, P. Capezzuto and G. Bruno, J. Vac. Sci. Technol. B, **20**, 1221 (2002).

²⁴S. D. Burnham, W. A. Doolittle, G. Namkoong and W. Henderson, J. Cryst. Growth, **279**, 26 (2005).

²⁵ASTM Standard F76, "Test Methods for Measuring Resistivity and Hall Coefficient and Determining Hall Mobility in Single-Crystal Semiconductors," ASTM International, West Conshohocken, PA, 2011.

²⁶R. R. Lieten, V. Motsnyi, L. Zhang, K. Cheng, M. Leys, S. Degroote, G. Buchowicz, O. Dubon and G. Borghs, J. Phys. D: Appl. Phys., **44**, 1345406 (2011).

²⁷H. Heinke, V. Kirchner, S. Einfeldt and D. Hommel, Appl. Phys. Lett., **77**, 2145 (2000).

²⁸J. Pereiro, A. Redondo-Cubero, S. Fernandez-Garrido, C. Rivera, A. Navarro, E. Muñoz, E. Calleja and R. Gago, J. Phys. D: Appl. Phys., **43**, 335101 (2010).

²⁹M. Lachab, D. H. Youn, R. S. Q. Fareed, T. Wang and S. Sakai, Solid State Electron., **44**, 1669 (2000).

³⁰J. Simon and D. Jena, Phys. Status Solidi A, **205**, 1074 (2008).

³¹D. K. Schroder, *Semiconductor Material and Device Characterization*, Third Ed. (J. Wiley, New York, 2006), 466-479.

³²N. F. Mott, Rev. Mod. Phys., **40**, 677 (1968).

³³N. F. Mott and W. D. Twose, Adv. Phys., **10**, 107 (1961).

³⁴D. C. Look, D. C. Reynolds, J. W. Hemsky, J. R. Sizelove, R. L. Jones and R. J. Molnar, Phys. Rev. Lett., **79**, 2273 (1997).

III. Transmission Electron Microscopy Analysis of High Indium Content InGaN

Introduction

The study of high-indium content InGaN systems is crucial for the development of longer wavelength III-nitride electronic devices. Achieving high quality InGaN layers is difficult since they are typically grown under conditions far from equilibrium. InGaN crystalline quality is severely affected by the large lattice mismatch ($\sim 10.6\%$) between GaN and InN with a strong tendency towards phase separation. In theory, InGaN alloys possess a miscibility gap where phase separation is inevitable due to spinodal decomposition.¹ However, it has been demonstrated that high-quality phase-separation-free InGaN layers can be obtained for a large range of indium contents.² The growth technique and temperature, strain, and thermal history have also shown to be linked to phase separation.³⁻⁵ The growth of high indium-content InGaN films strongly depends on temperature. The molecular beam epitaxy (MBE) technique can grow InGaN films at relatively low temperatures (400-600°C). Using a modified MBE technique known as metal-modulated epitaxy (MME)⁶ where the metal flux is shuttered at a modulated pattern while the nitrogen flux is kept constant, has shown improved material quality due to its enhanced surface adlayer diffusion.⁷

Strain also plays an important role in the suppression of phase separation.^{3,4,8} Thick $\text{In}_x\text{Ga}_{1-x}\text{N}$ layers have been shown to grow with no phase separation up to $x < 0.3$ but strained GaN/ $\text{In}_x\text{Ga}_{1-x}\text{N}$ /GaN double heterostructures exhibit no phase separation up to $x < 0.8$.³ On the other hand, it has been demonstrated that fully relaxed InGaN layers exhibit better crystalline quality. Relaxation of InGaN layers grown on GaN can be achieved by the introduction of misfit dislocations at the heterointerface.⁹ In *c*-plane film growth, these dislocations can be introduced by glide from the surface via active $\{11\bar{2}2\}\{11\bar{2}3\}$ slip planes as well as by edge- or mixed-type threading dislocations coming from the GaN underlayer.¹⁰ It has been reported that a critical thickness in InGaN layers is needed for the formation of arrays of misfit dislocations at the InGaN/GaN interfaces.¹⁰ These arrays have a six-fold symmetry due to their wurtzite crystal nature.

In this letter, we describe the structural and optical properties of thick InGaN layers with high-indium content grown by metal-modulated epitaxy (MME). Transmission electron microscopy (TEM) images show the appearance of Moiré fringes indicating a complete misfit strain relaxation at the InGaN/GaN interfaces. Two-beam diffraction-contrast TEM images taken at $\mathbf{g} = [0001]$, $[1\bar{1}00]$, and $[11\bar{2}0]$ reveal that the *c*-planes of the InGaN layer are parallel to the underlying GaN layer and exhibit slight crystal rotations about the *c*-axis. Photoluminescence (PL) measurements exhibit a single peak at 1300 nm corresponding to an $\text{In}_x\text{Ga}_{1-x}\text{N}$ layer with $x \sim 75\%$ in agreement with x-ray diffraction (XRD) patterns. TEM, PL, and XRD measurements confirm that InGaN layers grown by MME are relaxed and do not present phase separation. The high crystal quality is attributed to low growth temperature and enhanced surface adlayer diffusion, properties of the MME growth technique.

Experimental

The sample in this study consists of a thick wurtzite $\text{In}_x\text{Ga}_{1-x}\text{N}$ layer with a target indium content of $x \sim 75\%$ grown on a GaN template. Details of the growth parameters used in this study can be found elsewhere.⁷ The sample structure was capped with a 10-nm-thick GaN layer to protect the InGaN film. Cross-sectional samples were prepared for TEM by standard polishing followed by argon-ion-beam milling. The microstructure was analyzed in a JEOL 4000 TEM operated at 400kV. The thickness of the InGaN layer is ~ 50 nm determined from high-resolution TEM images.

Results and Discussion

Figure 1 shows the microstructure as observed by TEM along a $\langle 11\bar{2}0 \rangle$ projection. Figure 1(a) is a cross-section two-beam image with the \mathbf{g} vector parallel to the growth direction, $\mathbf{g} = [0001]$. The bottom InGaN/GaN interface is flat whereas the upper interface appears undulated. The period and amplitude of the sinusoidal undulation along the interface is ~ 45 nm and 5 nm, respectively. A correlation between dislocation propagation velocities and the surface morphology has been observed in SiGe/Si(100) systems.¹¹ The InGaN film exhibits bright and dark regions due to thickness contour effects.

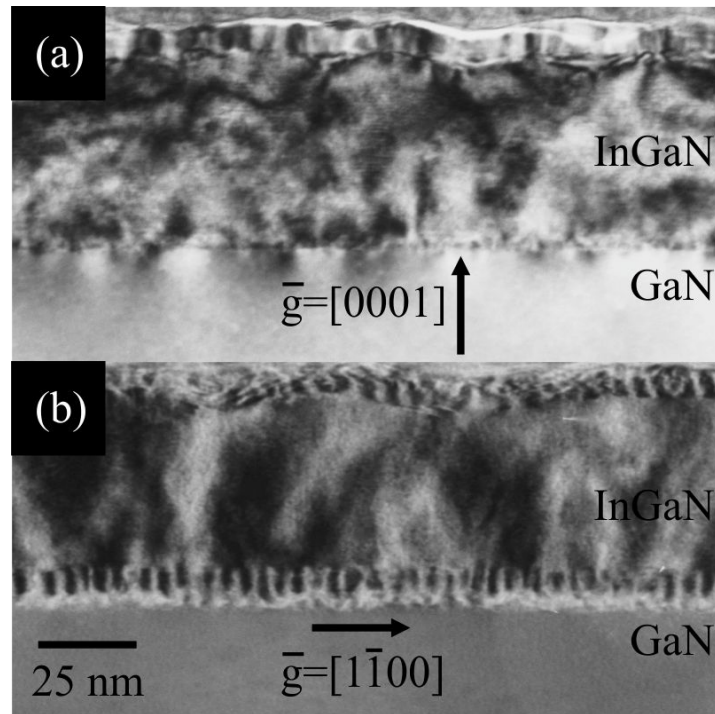


Figure 1. Microstructure of InGaN film, viewed by TEM in cross-section along the $\langle 11\bar{2}0 \rangle[\bar{1}120]$ projection, with diffraction contrast set at (a) $\mathbf{g} = (0001)$, and (b) $\mathbf{g} = (1\bar{1}00)$.

In order to observe misfit dislocations at the InGaN/GaN interfaces, the sample was tilted so that $\mathbf{g} = [1100]$, as shown in Fig. 1(b). The appearance of dark and bright lines at the InGaN/GaN interfaces is due to Moiré fringes, which indicates the existence of misfit

dislocations. The distance D between two dark fringes (~ 3.125 nm in the bottom interface) is related to the difference of similar equidistant planes by the equation:

$$D = \frac{d_{\text{GaN}}}{d_{\text{InGaN}} - d_{\text{GaN}}} \quad \text{Eq. 1}$$

where d_{GaN} and d_{InGaN} are the distances between sets of planes. The Moiré fringes were observed in the $\langle 11\bar{2}0 \rangle \langle 11\bar{2}0 \rangle$ zone-axis, thus $d = a\sqrt{d} = a\sqrt{a}$ where a is the lattice parameter on the basal plane. Using Eq. (1) and the above relations, we find $\Delta a = a_{\text{InGaN}} - a_{\text{GaN}} = 0.027 \pm 0.001 \text{ nm}$. This corresponds to an indium content in the InGaN layer of $\sim 77 \pm 4 \%$. These results indicate that the InGaN layer underwent a complete misfit strain relaxation within a few monolayers of the initial growth.

Fig. 2 shows cross-section TEM images taken along the $\langle 1\bar{1}00 \rangle$ zone-axis. Under $\mathbf{g} = [0001]$, we observe similar surface undulations as in Fig. 1(a). Undulations along two orthogonal projections, Figs. 1 and 2, indicate that the surface presents hillocks separated by ~ 45 nm along $\langle 11\bar{2}0 \rangle$ directions. Undulations are formed on the surface after a strain relaxation mechanism. First, the formation of surface steps are originated by glide of dislocations which later become misfit dislocations. Secondly, subsequent film growth via step elimination results in the observed undulations.¹² In addition, alternating bright and dark regions across the InGaN layer are observed under $\mathbf{g} = [11\bar{2}0]$ in Fig. 2(b), which indicates that the InGaN layer grows in columns with a slight crystal rotation about the c -axis. It should be noted that the width of each column is similar to the InGaN layer thickness. The in-plane twist observed here may be associated to a spiral growth which leads to phase separation.¹³ The possibility of phase separation in the InGaN layer will be discussed later.

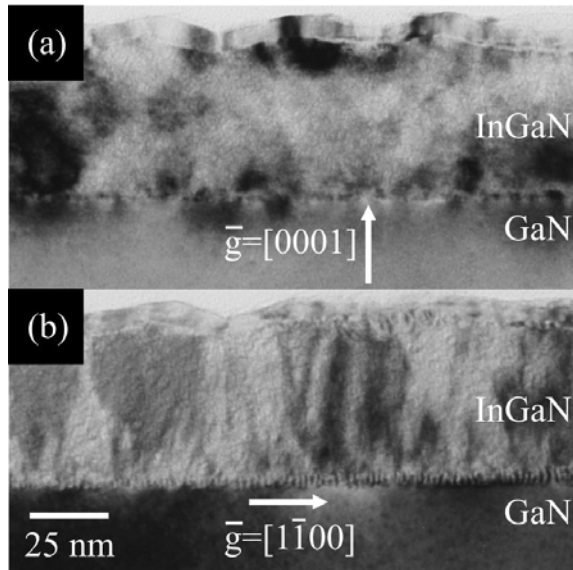


Figure 2. Microstructure of InGaN film, viewed in cross-section along the $\langle 1\bar{1}00 \rangle$ projection, with diffraction contrast set at (a) $\mathbf{g} = (0001)$, and (b) $\mathbf{g} = (11\bar{2}0)$.

Fig. 3 shows a high-resolution TEM image of the structure taken along the $\langle 11\bar{2}0 \rangle$ projection. We observe a few dark vertical lines in the InGaN layer. They are possibly dislocations formed at the columnar boundaries seen in Fig. 2(b). The *c*-planes of the InGaN layer are parallel to the GaN underlayer demonstrating good crystalline quality. We observed that for every 39 $\langle 1\bar{1}00 \rangle$ planes in the GaN layer, there are 36 $\langle 1\bar{1}00 \rangle$ planes in the InGaN layer, as indicated by the arrows. The difference in lattice parameter between these two layers is then

$$\Delta a = a_{\text{InGaN}} - a_{\text{GaN}} = \frac{39}{36} a_{\text{GaN}} - a_{\text{GaN}} = \frac{1}{12} a_{\text{GaN}} = 0.0265 \text{ nm}$$

$$\Delta a = a_{\text{InGaN}} - a_{\text{GaN}} = \frac{39}{36} a_{\text{GaN}} - a_{\text{GaN}} = \frac{1}{12} a_{\text{GaN}} = 0.0265 \text{ nm}$$

which is similar to the value obtained from the Moiré fringes analysis in Fig. 1(b). This confirms that the InGaN layer is completely relaxed on the GaN underlayer and with an indium content of $\sim 75\%$.

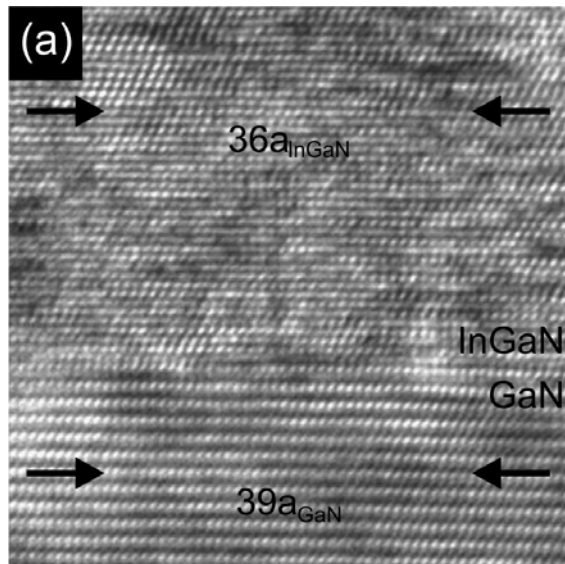


Figure 3. TEM lattice image of the InGaN/GaN interface, viewed along the $\langle 11\bar{2}0 \rangle$ projection.

We now focus on the possible phase separation for such high indium content InGaN layer. Fig. 4 shows an XRD diffraction scan of the structure for the $\langle 0002 \rangle$ diffraction spot. The InGaN peak is centered at $2\theta = 32.25^\circ$. No additional peaks are observed which indicate the absence of phase separation. The FWHM of the $\langle 0002 \rangle$ rocking curve of the InGaN layer shown in the inset is ~ 367 arcsec and compares to the one of the GaN layer (not shown here), thus reflecting a good crystalline quality. In order to analyze the luminescence characteristics of the InGaN layer, four Gaussian curves were fitted in the photoluminescence spectrum taken at 10 K as shown in Fig. 5. The dominant emission (blue dotted line) centered at ~ 1300 nm is attributed to the InGaN layer and the remaining peaks are associated to Fabry-Pérot fringes generated by the 4-um-thick GaN layer. The InGaN emission wavelength corresponds to an indium content of $\sim 76 \pm 2\%$ when using a bowing parameter of $b = 2.5$.

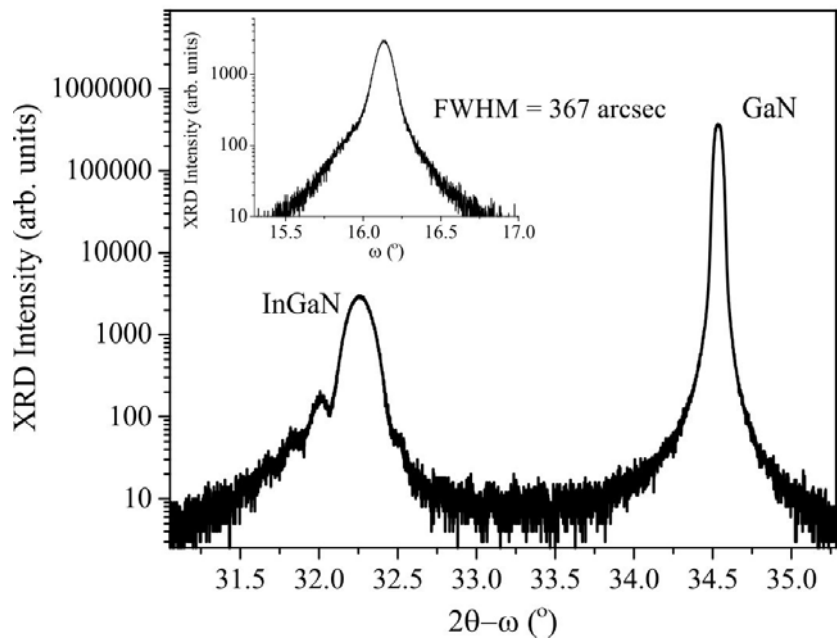


Figure 4. X-ray diffraction rocking curve ($2\theta-\omega$) for the (0002) diffraction peak.

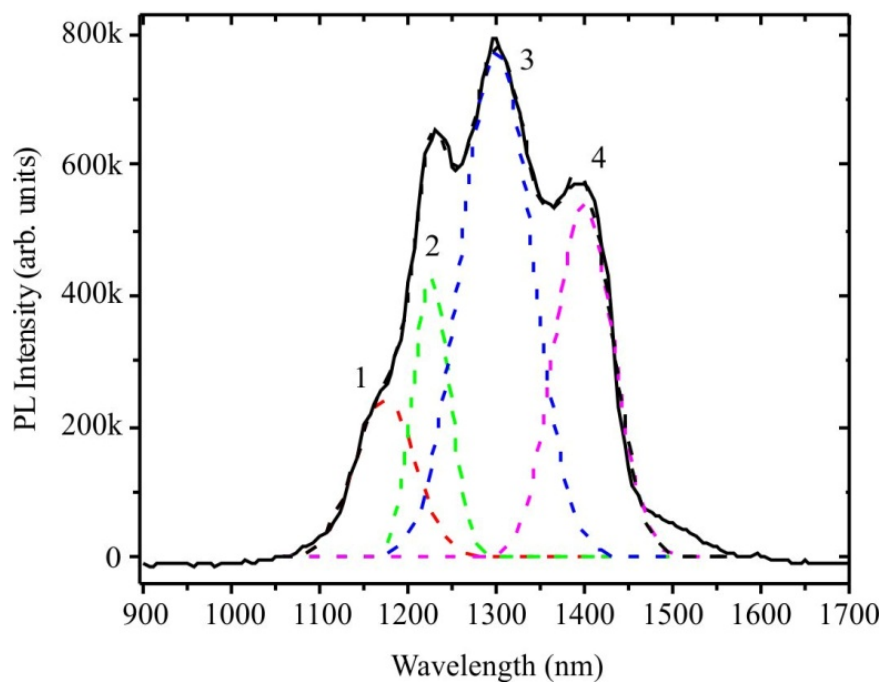


Figure 5. Photoluminescence spectrum of the InGaN layer taken at 4K. The spectrum is well fitted by four gaussian peaks.

REFERENCES

1. I. Ho and G. B. Stringfellow, *Appl. Phys. Lett.* **69**, 2701 (1996).
2. R. Singh, D. Doppalapudi, T. D. Moustakas, and L. T. Romano, *Appl. Phys. Lett.* **70**, 1089 (1997).
3. N. A. El-Masry, E. L. Piner, S. X. Liu, and S. M. Bedair, *Appl. Phys. Lett.* **72**, 40 (1998).
4. D. Doppalapudi, S. N. Basu, K. F. Ludwig Jr., and T. D. Moustakas, *J. Appl. Phys.* **84**, 1389 (1998).
5. Y.-T. Moon, D.-J. Kim, K.-M. Song, I.-H. Lee, M.-S. Yi, D.-Y. Noh, C.-J. Choi, T.-Y. Seong, and S.-J. Park, *Phys. Stat. Sol B* **216**, 167 (1999).
6. S. D. Burnham and W. A. Doolittle, *J. Vac. Sci. Technol. B* **24**, 2100 (2006).
7. M. Moseley, J. Lowder, D. Billingsley, and W. A. Doolittle, *App. Phys. Lett.* **97**, 191902 (2010).
8. A. Tabata, L. K. Teles, L. M. R. Scolfaro, J. R. Leite, A. Kharchenko, *Appl. Phys. Lett.* **80**, 769 (2002).
9. J. W. Matthews and A. E. Blakeslee, *J. Cryst. Growth* **27**, 118 (1974).
10. F. A. Ponce, S. Srinivasan, A. Bell, L. Geng, R. Liu, M. Stevens, J. Cai, H. Omiya, H. Marui, and S. Tanaka, *Phys. Stat. Sol A* **240**, 273 (2003).
11. C.-C. Wu, E. A. Stach, and R. Hull, *Nanotech.* **18**, 167505 (2007).
12. T. Sugahara, M. Hao, T. Wang, D. Nakagawa, Y. Naoi, K. Nishino, and S. Sakai, *Jpn. J. Appl. Phys.* **37**, L1195 (1998).

CONCLUSION

Metal-modulated epitaxy of InGaN has been investigated. A model has been developed regarding adlayer buildup and indium surface segregation based on RHEED patterns and transient RHEED intensities. This model was strengthened by a quantification of the indium surface segregation onset dose, which is found to be a value less than 2ML. Since a minimum of 2.3 ML of excess metal will accumulate in metal-rich, non-shuttered growth of InGaN, some form of modulation will be required in order to suppress indium surface segregation while obtaining high-quality growth. Finally, these theories were tested by growing InGaN samples with varying compositions. Single-phase, high quality InGaN with compositions throughout the miscibility gap and RMS roughnesses less than 0.8 nm were obtained demonstrating the feasibility of shuttered, metal-rich InGaN growth.

p-type GaN:Mg films have been grown using Metal-Modulated Epitaxy with varied Ga and Mg flux on c-plane sapphire substrates. A resistivity of $0.30 \Omega\text{-cm}$ and hole concentration of $5.1 \times 10^{18} \text{ cm}^{-3}$ have been demonstrated at cryogenic temperatures and $1.9 \times 10^{19} \text{ cm}^{-3}$ and $0.19 \Omega\text{-cm}$ at room temperature. In contrast, a lighter doped film exhibited resistivity of $146 \Omega\text{-cm}$ and donor-compensated conductivity at cryogenic temperatures. Temperature dependent Hall effect analysis of the heavily doped MME-grown film indicates Mg effective activation energies as low as 43 meV which varied with hole concentration supporting the conclusion of the formation of an energy band whose energy splitting is concentration dependent. Finally, a Mg acceptor ionization efficiency of 52% has been demonstrated by comparing the SIMS depth profile to carrier concentration. Overall, the electrical properties of the highly doped film and the negligible temperature dependent behavior point to impurity band conduction as the primary mechanism explaining these results.

We have also reported on the optical and structural properties of a thick $\text{In}_{0.76}\text{Ga}_{0.24}\text{N}$ layer grown by metal-modulated epitaxy. A two-beam diffraction condition TEM image exhibits Moiré fringes at the InGaN/GaN interfaces and missing $(\mathbf{1100})$ planes in the InGaN layer indicate that the InGaN layer experiences a complete misfit strain relaxation at the early stages of growth. Despite of the good parallelism of the basal planes between the InGaN and GaN layers, a slight in-plane misorientation along the *c*-axis is observed represented by the change of contrast under $\mathbf{g} = [\mathbf{1120}]$ conditions. The crystal domains have a width similar to the thickness of the InGaN layer. Finally, XRD and PL measurements revealed that the InGaN layer does not exhibit phase separation. The indium content in the InGaN layer is estimated at $\sim 76\%$ and agrees with the microstructural and optical analysis reported here.